



1 Comparative assessment of TROPOMI and OMI formaldehyde 2 observations against MAX-DOAS network column measurements.

3 Isabelle De Smedt¹, Gaia Pinardi¹, Corinne Vigouroux¹, Steven Compernelle¹, Alkis Bais², Nuria
4 Benavent³, Folkert Boersma^{4,5}, Ka-Lok Chan⁶, Sebastian Donner⁷, Kai-Uwe Eichmann⁸, Pascal
5 Hedelt⁶, François Hendrick¹, Hitoshi Irie⁹, Vinod Kumar⁷, Jean-Christopher Lambert¹, Bavo
6 Langerock¹, Christophe Lerot¹, Cheng Liu¹⁰, Diego Loyola⁶, Ankie PETERS⁴, Andreas Richter⁸,
7 Claudia Rivera Cárdenas¹¹, Fabian Romahn⁶, Robert George Ryan^{12,13}, Vinayak Sinha¹⁴, Nicolas
8 Theys¹, Jonas Vlietinck¹, Thomas Wagner⁷, Ting Wang¹⁵, Huan Yu¹, Michel Van Roozendael¹.

9 *Correspondence to:* Isabelle De Smedt (isabelle.desmedt@aeronomie.be)

- 10 1. Royal Belgian Institute for Space Aeronomy (BIRA-IASB), Ringlaan 3, 1180 Uccle, Belgium.
11 2. Laboratory of Atmospheric Physics, Aristotle University of Thessaloniki (AUTH), Thessaloniki, Greece.
12 3. Department of Atmospheric Chemistry and Climate, Institute of Physical Chemistry Rocasolano (CSIC), Madrid,
13 Spain.
14 4. Royal Netherlands Meteorological Institute (KNMI), De Bilt, the Netherlands.
15 5. Meteorology and Air Quality group, Wageningen University, the Netherlands.
16 6. Institut für Methodik der Fernerkundung (IMF), Deutsches Zentrum für Luft und Raumfahrt (DLR),
17 Oberpfaffenhofen, Germany.
18 7. Max-Planck-Institut für Chemie (MPI-C), Mainz, Germany.
19 8. Institute of Environmental Physics, University of Bremen (IUP-B), Bremen, Germany.
20 9. Center for Environmental Remote Sensing, Chiba University (Chiba U), Chiba, Japan
21 10. Department of Precision Machinery and Precision Instrumentation, University of Science and Technology of
22 China, Hefei, China.
23 11. Centro de Ciencias de la Atmósfera, Universidad Nacional Autónoma de México (UNAM), Mexico City, Mexico
24 12. School of Earth Sciences, The University of Melbourne, Melbourne, Australia
25 13. ARC Centre of Excellence for Climate System Science, Sydney, Australia
26 14. Department of Earth and Environmental Sciences, Indian Institute of Science Education and Research (IISER),
27 Mohali, India
28 15. Institute of Atmospheric Physics, Chinese Academy of Sciences (CAS), Beijing, China
29

30 **Abstract.** The TROPOspheric Monitoring Instrument (TROPOMI), launched in October 2017 on board the Sentinel-
31 5 Precursor (S5P) satellite, monitors the composition of the Earth's atmosphere at an unprecedented horizontal
32 resolution as fine as 3.5x5.5 km². This paper assess the performances of the TROPOMI formaldehyde (HCHO)
33 operational product compared to its predecessor, the OMI HCHO QA4ECV product, at different spatial and temporal
34 scales. The parallel development of the two algorithms favored the consistency of the products, which facilitates the
35 production of long-term combined time series. The main difference between the two satellite products is related to the
36 use of different cloud algorithms, leading to a positive bias of OMI compared to TROPOMI of up to 30% in Tropical
37 regions. We show that after switching off the explicit correction for cloud effects, the two datasets come into an
38 excellent agreement. For medium to large HCHO vertical columns (larger than 5x10¹⁵ molec.cm⁻²) the median bias
39 between OMI and TROPOMI HCHO columns is not larger than 10% (<0.4x10¹⁵ molec.cm⁻²). For lower columns,
40 OMI observations present a remaining positive bias of about 20% (<0.8x10¹⁵ molec.cm⁻²) compared to TROPOMI in
41 mid-latitude regions. Here, we also use a global network of 18 MAX-DOAS instruments to validate both satellite
42 sensors for a large range of HCHO columns. This work complements the study by Vigouroux et al. (2020) where a



43 global FTIR network is used to validate the TROPOMI HCHO operational product. Consistent with the FTIR
44 validation study, we find that for elevated HCHO columns, TROPOMI data are systematically low (-25% for HCHO
45 columns larger than 8×10^{15} molec.cm⁻²), while no significant bias is found for medium range column values. We
46 further show that OMI and TROPOMI data present equivalent biases for large HCHO levels. However, TROPOMI
47 significantly improves the precision of the HCHO observations at short temporal scales, and for low HCHO columns.
48 We show that compared to OMI, the precision of the TROPOMI HCHO columns is improved by 25% for individual
49 pixels, and up to a factor 3 when considering daily averages in 20km-radius circles. The validation precision obtained
50 with daily TROPOMI observations is comparable to the one obtained with monthly OMI observations. To illustrate
51 the improved performances of TROPOMI in capturing weak HCHO signals, we present clear detection of HCHO
52 column enhancements related to shipping emissions in the Indian Ocean. This is achieved by averaging data over a
53 much shorter period (3 months) than required with previous sensors, and opens new perspectives to study shipping
54 emissions of VOCs and related atmospheric chemical interactions.

55 1 Introduction

56 Satellite observations of tropospheric formaldehyde (HCHO) columns have been used for years to support air quality
57 and chemistry-climate related studies from the regional to the global scale. Formaldehyde is an intermediate gas in
58 almost all oxidation chains of non-methane volatile organic compounds (NMVOC), leading to the production of CO,
59 and eventually CO₂. NMVOCs are, together with NO_x, CO and CH₄, among the most important precursors of
60 tropospheric ozone. NMVOCs also produce secondary organic aerosols and influence the concentrations of OH, the
61 main tropospheric oxidant. The major HCHO source in the remote atmosphere is CH₄ oxidation. Over the continents,
62 the oxidation of other NMVOCs emitted from vegetation, fires, traffic and industrial sources results in important and
63 localised enhancements of the HCHO levels. Because its short lifetime (of the order of a few hours), HCHO in the
64 boundary layer can be related to the release of a large number of short-lived volatile hydrocarbons. Furthermore,
65 HCHO observations provide information on the chemical oxidation processes in the atmosphere, including CO
66 chemical production from CH₄ and NMVOC, the oxidation of isoprene into HCHO, which allows quantification of
67 midday OH (Wells et al., Nature, 2019), and the tropospheric ozone production regimes that depend on the HCHO to
68 NO₂ ratios (Jin et al., 2020).

69 Satellite observations of formaldehyde columns in the troposphere have been extensively reported in the literature
70 from a number of nadir UV sensors, e.g.: Global Ozone Monitoring Experiment (GOME; Chance et al., 2000; Palmer
71 et al., 2001; De Smedt et al., 2008), SCanning Imaging Absorption spectroMeter for Atmospheric CHartographY
72 (SCIAMACHY; Wittrock et al., 2006; De Smedt et al., 2008; 2010), Ozone Monitoring Instrument (OMI; González
73 Abad et al., 2015; De Smedt et al., 2015; 2018; Kaiser et al. 2018; Levelt et al., 2018), Global Ozone Monitoring
74 Experiment-2 (GOME-2; De Smedt et al., 2012; 2015; Vrekoussis et al., 2010; Hewson et al., 2013; Hassinen et al.,
75 2016), and Ozone Mapping and Profiler Suite (OMPS; Li et al., 2015; González Abad et al., 2016). They are used in
76 many studies related to air quality and climate change (e.g. Stavrakou et al., 2014; 2015; 2016; 2018; Fortems-Cheiney
77 et al., 2012; Marais et al., 2012; Mahajan et al., 2015; Choi et al., 2015; Zhu et al., 2016; Chan Miller et al., 2017; Jin



78 et al., 2017; Barkley et al., 2017; Cao et al., 2018; Khan et al., 2018; Surl et al., 2018; Shen et al. 2019; Su et al.; 2019;
79 Zyrichidou et al., 2019; Jin et al., 2020; Sourì et al., 2020; Wells et al., 2020; Franco et al., 2021; Opacka et al., 2021).
80 Launched on board of the European Copernicus Sentinel-5 Precursor (S5P) satellite on 13 October 2017, the
81 TROPospheric Monitoring Instrument (TROPOMI, Veeffind et al., 2012) is designed for the daily monitoring of the
82 troposphere at the global scale. Compared to its predecessor OMI, its spatial resolution is about 16 times better with
83 at least the same signal to noise ratio per ground pixel. The improved TROPOMI capabilities for the observation of
84 HCHO have been illustrated for the detection of fire plumes and their transport (Alvarado et al., 2020; Theys et al.
85 2020), and the detection of rapid changes in anthropogenic emissions related to the COVID crisis in China and India
86 (Levelt et al., 2021; Sun et al. 2021). The TROPOMI observations extend the historical time series of midday
87 observations performed using OMI. Both datasets are used in combination for long-term trend studies (Li et al., 2020).
88 It is therefore important to evaluate their level of agreement and to report on the best practices to combine datasets
89 from different sensors.

90 The TROPOMI vertical column product requirements specify a single measurement precision of 12×10^{15} molec.cm²,
91 4×10^{15} molec.cm² at 20km spatial resolution, and a systematic uncertainty lower than 40%-80% (ESA, 2014). The
92 Copernicus user requirements, primarily defined for NMVOC measurements, are more stringent. For the
93 environmental air quality theme, the required maximum uncertainty is defined as 60% or 1.3×10^{15} molec.cm² (least
94 stringent), at the spatial resolution of 20km and with a revisit time of 2 hours. The space and time resolution are less
95 stringent for the climate theme (30% or 1.3×10^{15} molec.cm², 50km, 3 days) (Bovensmann et al., 2011; Langen et al.,
96 2017).

97 Given these rather strict product requirement and the diversity of the NMVOC species, lifetimes and sources (biogenic,
98 biomass burning or anthropogenic), a validation approach addressing a large variety of conditions worldwide (tropical,
99 temperate and boreal forests, urban and sub-urban areas) is needed, as well as continuous measurements in order to
100 obtain good statistics and capture the seasonal variations. Vigouroux et al. (2020) validated the operational TROPOMI
101 HCHO product using a global network of Fourier Transform Infrared (FTIR) instruments. The study concluded that
102 overall the HCHO product fulfils the requirements of the TROPOMI mission. Compared to the FTIR data, the
103 TROPOMI HCHO columns present a negative bias over high emission sites (-31% for HCHO columns larger than
104 8×10^{15} molec.cm²) and a positive bias for clean sites (+26% for HCHO columns lower than 2.5×10^{15} molec.cm²).
105 Based on clean sites, an upper limit of 1.3×10^{15} molec.cm² was estimated for the deviation of daily observations at a
106 spatial resolution of 20km. It was also pointed out that this level of random uncertainty, although reaching the
107 Copernicus user requirements, is about twice as large as the expected theoretical noise (individual pixel precision
108 divided by the square root of the number of observations). However, Vigouroux et al. (2020) do not address the
109 consistency of TROPOMI HCHO with other satellite products and MAX-DOAS HCHO observations.

110 The present paper is a follow-up of De Smedt et al. (2018), where the HCHO retrieval algorithm applied to both OMI
111 and TROPOMI sensors was presented. Here we concentrate on a global study of three years of HCHO observations
112 with TROPOMI, and we analyse their consistency with OMI data. Throughout the paper, we discuss the improved
113 capabilities of TROPOMI for the detection of HCHO at different temporal and spatial scales, from background
114 conditions to high emissions. We start with a few illustrations of the TROPOMI capabilities for HCHO monitoring



115 from space (sect. 3). We then provide a detailed comparison with the OMI QA4ECV HCHO dataset (sect. 4). In sect.
116 5, a global network of MAX-DOAS instruments is used to validate the OMI and TROPOMI HCHO datasets. Finally,
117 in sect. 6, we illustrate the enhanced capability of TROPOMI for the detection of very small HCHO emissions with
118 the identification of a signal over shipping lanes in the Indian Ocean.

119 2 HCHO Datasets

120 2.1 OMI instrument and QA4ECV HCHO product

121 The Aura satellite was launched in July 2004, in a low-Earth polar orbit crossing the equator at 13:30 LT. On board
122 of Aura, the Ozone Monitoring Instrument (OMI) is a nadir viewing imaging spectrometer that measures the solar
123 radiation backscattered by the Earth's atmosphere and surface over the wavelength range from 270 to 500 nm (Levelt
124 et al., 2006). Operational Level 2 (L2) products include vertical columns of O₃, SO₂, NO₂, HCHO, BrO, OCIO, as
125 well as cloud and aerosol information. OMI has a 2600 km wide swath (divided into 60 across-track positions or
126 rows), providing near-daily global coverage. However, due to a detector row anomaly that occurred after a few years
127 of operation, an increasing number of rows had to be filtered out leading to gradual degradation of the coverage. The
128 OMI ground pixel size varies from 13x24 km² at nadir to 28x150 km² at the edges of the swath.

129 The OMI QA4ECV HCHO product was developed by a European consortium (BIRA, IUP, MPIC, KNMI, WUR) (De
130 Smedt et al., 2017, <http://doi.org/10.18758/71021031>) in the framework of the EU-FP7 QA4ECV project. A detailed
131 step-by-step study was performed for HCHO and NO₂ retrievals as part of a community effort to homogenize GOME,
132 SCIAMACHY, GOME-2 and OMI, leading to state-of-the art European products (www.qa4ecv.eu). For this study,
133 we use the version 1.2 of the OMI HCHO dataset that is now spanning 15 years (2005-2020; Boersma et al., 2018;
134 Lorente et al., 2017; Nightingale et al., 2018; Zara et al., 2018). Note that within QA4ECV, a homogenized dataset of
135 NO₂ and HCHO MAX-DOAS reference measurements (QA4ECV_MAXDOAS) was also developed for satellite
136 validation (see sect. 2.4 and sect. 5).

137 2.2 TROPOMI instrument and the HCHO operational product

138 On board of the S5P platform, which - like Aura - flies in a low-Earth afternoon polar orbit with a local overpass time
139 of 13:30, the TROPOMI instrument is based on an imaging spectrometer measuring in the ultraviolet (UV), visible
140 (VIS), near-infrared (NIR), and shortwave infrared (SWIR) spectral regions (Veefkind et al., 2012). Operational L2
141 products include vertical columns of O₃, SO₂, NO₂, HCHO, CO and CH₄, as well as cloud and aerosol information.
142 TROPOMI has a 2600 km wide swath (divided into 450 across-track positions or rows), providing near-daily global
143 coverage. The spatial resolution at nadir, originally of 3.5x7 km² (across-track x along-track) has been refined to
144 3.5x5.5 km² on 6 August 2019, by a change in the along-track integration time. The size of the pixels remains more
145 or less constant towards the edges of the swath (the largest pixels are ~14 km wide) (L1b ATBD, L1b readme file).

146 The retrieval algorithm of the TROPOMI HCHO L2 product is directly inherited from the QA4ECV OMI algorithm
147 with the aim to create a consistent time series of early afternoon observations. For this study, we use a modified version
148 of the TROPOMI level-2 HCHO operational data product, which starts in April 2018 (phase E2, RPRO+OFFL,



149 product versions 1.1.[5-8]+2.1.3, doi: 10.5270/S5P-tjlxfd2). Product versions are described in the [Product Readme](#)
150 [File](#).

151 2.3 HCHO Retrieval algorithm for OMI and TROPOMI

152 The HCHO retrieval algorithm was fully described in De Smedt et al. (2018), and the successive adaptations of the
153 algorithm are reported in the S5P product ATBD. Here we only provide a short description of the algorithm, which is
154 based on a 3-steps DOAS method. First, the fit of the slant columns (N_s) is performed in the UV part of the spectra,
155 in the fitting interval 328.5-359 nm. The HCHO cross-section is from Meller and Moortgat (2000). All cross-sections
156 have been pre-convolved for every row separately with an instrumental slit function adjusted after TROPOMI launch.
157 For the OMI product, the slit function of each row is adjusted daily and the cross-sections are reconvolved accordingly.
158 The DOAS reference spectrum is updated daily with an average of Earth radiances measured in the Equatorial Pacific
159 region from the previous day. The fit therefore results in a differential slant column, corresponding to the HCHO
160 excess over sources compared to the remote background. In a second step, the conversion from slant to tropospheric
161 vertical columns (N_v) is performed using a look up table of vertically resolved air mass factors (M) calculated at 340
162 nm with the radiative transfer model VLIDORT v2.6 (Spurr, 2008). Entries for each ground pixel are the observation
163 geometry, the surface elevation and reflectivity, as well as clouds treated as reflecting surfaces, and a priori
164 tropospheric HCHO profiles. The surface albedo is taken from the monthly OMI albedo climatology at the spatial
165 resolution of $1^\circ \times 1^\circ$ (minimum LER, Kleipool et al., 2008). A priori vertical profiles are provided by the TM5-MP
166 daily analysis, at the spatial resolution of $1^\circ \times 1^\circ$ (Williams et al., 2017). A cloud correction based on the independent
167 pixel approximation (Boersma et al., 2004) is applied for cloud fractions (CF) larger than 0.1. Finally, to correct for
168 any remaining global offset and possible stripes arising between the rows, a background correction is performed based
169 on the HCHO slant columns in the Pacific Ocean ($N_{s,0}$). For the TROPOMI operational product, $N_{s,0}$ is based on the
170 four previous days. For this study, and for the OMI product, we perform the correction on the current day in order to
171 further reduce the stripes. To compensate for a background HCHO level in the Equatorial Pacific (due to the methane
172 oxidation), a vertical column of HCHO ($N_{v,0}^{CTM}$) is taken from the TM5 model in the reference region. The resulting
173 tropospheric HCHO vertical column can be written as follows:

$$N_v = \frac{N_s - N_{s,0}}{M} + \frac{M_0}{M} N_{v,0}^{CTM}, \quad (2-1)$$

174 with M_0 the air mass factor in the reference sector. Intermediate quantities and auxiliary data are all stored in the L2
175 files (see the product user manual for TROPOMI and OMI). Several diagnostic variables are provided together with
176 the measurements. The column averaging kernels and the a priori profiles are given for each observation. The
177 tropospheric column uncertainty is resolved into its random (precision) and systematic components (accuracy), and is
178 provided for every individual pixel.

179 The main difference between the OMI and TROPOMI algorithms lies in the cloud product that is used to compute air
180 mass factors. While the QA4ECV OMI product is based on the O_2-O_2 absorption feature around 477 nm, and considers
181 a fixed cloud albedo of 0.8 (version 2.0, Veefkind et al., 2016), the TROPOMI product uses the S5P operational cloud
182 product in CRB (Cloud as Reflecting Boundary) mode (OCRA/ROCINN-CRB; Loyola et al., 2018). The S5P



183 ROCINN algorithm is based on the O₂ A-band around 760 nm and simultaneously retrieves cloud height and cloud
184 albedo. Systematic differences between the cloud parameters will result in differences in the air mass factors,
185 influencing the comparisons. To mitigate the impact of this difference between OMI and TROPOMI, we also switch
186 off the cloud correction by replacing the cloud-corrected AMF by an equivalent clear-sky AMF (M_{clear} , no cloud
187 correction applied) also provided in the L2 product. Based on equation (2-1), the following simple transformation can
188 be applied:

$$N_{v_clear} = \frac{M}{M_{clear}} N_v \quad (2-2)$$

189 Note that this transformation has an effect on observations with cloud fractions comprised between 0.1 and 0.4. Indeed,
190 no cloud correction is applied for $CF < 0.1$ and observations with $CF > 0.4$ are filtered out from the analysis.

191 2.4 MAX-DOAS datasets

192 Multi-axis DOAS (MAX-DOAS) instruments retrieve the abundance of atmospheric trace species in the lowermost
193 troposphere (Hönniger et al., 2004; Wagner et al., 2004; Wittrock et al., 2004; Heckel et al., 2005). Based on DOAS
194 analyses (Platt and Stutz, 2008) of the scattered sky light under different viewing elevations, high sensitivity close to
195 the surface is obtained for the smallest elevation angles, whereas measurements at higher elevations provide
196 information on the rest of the column. MAX-DOAS measurements have been used in several studies to validate
197 satellite HCHO columns (Vigouroux et al., 2009; Franco et al., 2015; De Smedt et al., 2015; Chan et al., 2019; 2020;
198 Ryan et al., 2020; Kumar et al. 2020). However, a global network of MAX-DOAS instruments has not been used yet
199 for the validation of HCHO columns from space.

200 Ground-based data used in this study are presented in Table 1. Apart from the QA4ECV MAX-DOAS dataset, which
201 relies on harmonized HCHO retrievals (Pinardi et al., 2013; QA4ECV [D3.8](#) and [D3.9](#),
202 <http://www.qa4ecv.eu/sites/default/files>), the MAX-DOAS data sets used here were generated by instrument principal
203 investigators using non-harmonised settings. The conversion to vertical columns and/or vertical profiles relies on
204 methods of various complexity levels. Table 1 includes details about the retrieval strategy adopted by the different
205 teams. These include:

- 206 • GA: Geometrical approximation, the vertical column is determined using a single-scattering approximation
207 adequate for moderately high elevation angles α (typically 30°) so that a simple geometrical air-mass factor
208 ($AMF \approx SCD/VCD = 1/\sin(\alpha)$) (Hönniger et al., 2004; Brinksma et al., 2008; Ma et al., 2013) can be used,
- 209 • QA4ECV: the vertical column is calculated using tropospheric AMFs based on climatological profiles and
210 aerosol loads as developed during the QA4ECV project ([QA4ECV MAXDOAS readme file](#)). These data are
211 less sensitive to relative azimuth angle than the purely geometric approximation presented above,
- 212 • OEM: Vertical profile algorithms using an Optimal Estimation Method (Rodgers, 2000): these make use of a-
213 priori vertical profiles and associated uncertainties (Friess et al., 2006; Clémer et al 2010; Hendrick et al., 2014;
214 Gielen et al., 2017; Wang et al., 2019a; Friedrich et al., 2019; Bösch et al., 2018),
- 215 • PP: Vertical profile algorithms based on parameterized profile shape functions: these make use of analytical
216 expressions to represent the trace gas profile using a limited number of parameters (Irie et al., 2009; 2011; Li et
217 al., 2010; Vlemmix et al., 2010; Wagner et al., 2011; Beirle et al., 2019).



218 Both OEM and parameterized profiling approaches provide vertical profiles of aerosols and HCHO with good
219 sensitivity in the 0-4 km altitude range, in which 1 to 3 independent pieces of information in the vertical dimension
220 are available (Vlemmix et al., 2015; Friess et al., 2016; 2019). Recent intercomparison studies (Vlemmix et al., 2015;
221 Friess et al., 2019; Tirpitz et al., 2021) show that both OEM and parameterized inversion approaches lead to consistent
222 results in terms of tropospheric vertical columns but to larger differences in terms of profiles. The accuracy of the
223 MAX-DOAS technique depends on the SCD retrieval noise, the uncertainty of the HCHO absorption cross-sections,
224 the choice of the a-priori profile shape and the uncertainty of the tropospheric AMF calculation. MAX-DOAS HCHO
225 slant columns from several instruments have been compared during international large-scale campaigns (CINDI-1 and
226 2, e.g. Pinardi et al., 2013; Kreher et al., 2020) showing relatively large median differences and larger noise compared
227 to other slant column products comparisons (e.g. NO₂). For HCHO, the slant column precision depends strongly on
228 the signal-to-noise performance of the DOAS instrument with significantly better results for low-noise research-grade
229 MAX-DOAS instruments (Pinardi et al., 2013; Kreher et al., 2020). The estimated total uncertainty on HCHO VCD
230 is of the order of 30% to 60% in polluted conditions. This includes both random (~5% to 30% depending on
231 instrumental signal-to-noise ratio) and systematic (20%) slant column contributions (Pinardi et al., 2013).

232 **Table 1: MAX-DOAS HCHO datasets included in the validation exercise. GA stands for geometrical approximation, OEM**
233 **for Optimal Estimation Method and PP for Parametrized Profiling.**

Station, Country (lat/long)	Owner/ Group	Instrument Type	Retrieval Type	Reference
De Bilt, The Netherlands (52.10°N, 5.18°E)	KNMI	miniDOAS / Airyx	SCD and VCD from QA4ECV	Vlemmix et al., 2010 QA4ECV
Cabauw, The Netherlands (51.97°N, 4.93°E)	KNMI	miniDOAS/ Hoffmann	SCD and VCD from QA4ECV	QA4ECV
Uccle, Belgium (50.78° N, 4.35° E)	BIRA-IASB	Custom-built MAX-DOAS	VCD and profiles from OEM	Dimitropoulou et al, 2020
Xianghe, China (39.75° N, 116.96° E)	BIRA-IASB	Custom-built MAX-DOAS	VCD and profiles from OEM	Hendrick et al., 2014; Vlemmix et al., 2015
Mainz, Germany (50°N, 8.2°E)	MPIC	Custom-built MAX-DOAS	SCD and VCD from QA4ECV	Wang et al., 2017 QA4ECV
Munich, Germany (48,13_N, 11.58°E)	LMU	Airyx 2D MAX-DOAS	VCD and profiles from OEM	Chan et al. 2020
Mohali, India (30.67°N, 76.74°E)	IISER/MPIC	Custom-built MAX-DOAS	SCD and VCD from QA4ECV	Kumar et al., 2020 QA4ECV
Thessaloniki, Greece (40.63°N, 22.96°E)	AUTH	Phaethon	SCD and VCD from QA4ECV	Drosoglou et al., 2017 QA4ECV
Madrid, Spain (40.3°N, 3.7°W)	CSIC	MAX-DOAS	VCD and profiles from OEM	Benavent, et al., 2019.
Fukue, Japan (36.8°N, 128.7°E)	ChibaU	CHIBA-U MAX- DOAS	VCD and profiles from PP	Irie et al., 2011; 2012; 2015; 2019.
Chiba, Japan (35.63°N, 140.10°E)	ChibaU	CHIBA-U MAX- DOAS	VCD and profiles from PP	Irie et al., 2011; 2012; 2015; 2019.
Kasuga, Japan	ChibaU	CHIBA-U MAX-	VCD and profiles from PP	Irie et al., 2011; 2012; 2015;



(33.52°N, 130.48°E)		DOAS		2019.
Pantnagar, India (29°N, 79.47°E)	ChibaU	CHIBA-U MAX-DOAS	VCD and profiles from PP	Irie et al., 2011; 2012; 2015; 2019.
Phimai, Thailand (15.18°N, 102.56°E)	ChibaU	CHIBA-U MAX-DOAS	VCD and profiles from PP	Irie et al., 2011; 2012; 2015; 2019.
Xianghe, China (39.75° N, 116.96° E)	USTC	MAX-DOAS	VCD from OEM	
Beijing CAMS, China, (39.95°N, 116.32°E)	USTC	MAX-DOAS	VCD from GA	
UNAM, Mexico (19.33°N, 99.18°W)	UNAM	MAX-DOAS	VCD and profiles from OEM Eastwards pointing	Rivera Cardenas et al., 2021 Arellano et al., 2016
BroadMeadows, Australia (-37.7°, 144.9°)	Melbourne University ABM	Airyx	VCD from OEM	Ryan et al. 2018; 2020.

234 2.5 Data Use and Method

235 For this study, unless specified otherwise, we filter the satellite data based on the quality assurance values (QA)
236 ([Product Readme File](#)). QA>0.5 filters out most observations presenting an error flag or a solar zenith angle larger
237 than 70°, a cloud radiance fraction (CRF) at 340 nm larger than 0.6, an air mass factor smaller than 0.1, surface
238 reflectivity larger than 0.2, or an activated snow/ice flag. It should be noted that, in the first versions of the operational
239 product, the QA values were not correctly assigned over snow/ice regions, above 75° of SZA, and sometimes over
240 cloudy scenes. This issue has been corrected from version 2.1.3 (July 2020). For this study, we therefore reassigned
241 QA values using the above-mentioned filters.

242 We calculated daily gridded data at a resolution of 0.05°x0.05° in latitude/longitude, both for OMI and TROPOMI,
243 using the [Harp atmospheric toolbox](#). Along the paper, daily and monthly averages are obtained from daily grids. For
244 each day, we require the region to be filled with a least 50% of valid grid cells, with a minimum of 10 TROPOMI
245 observations (2 OMI observations).

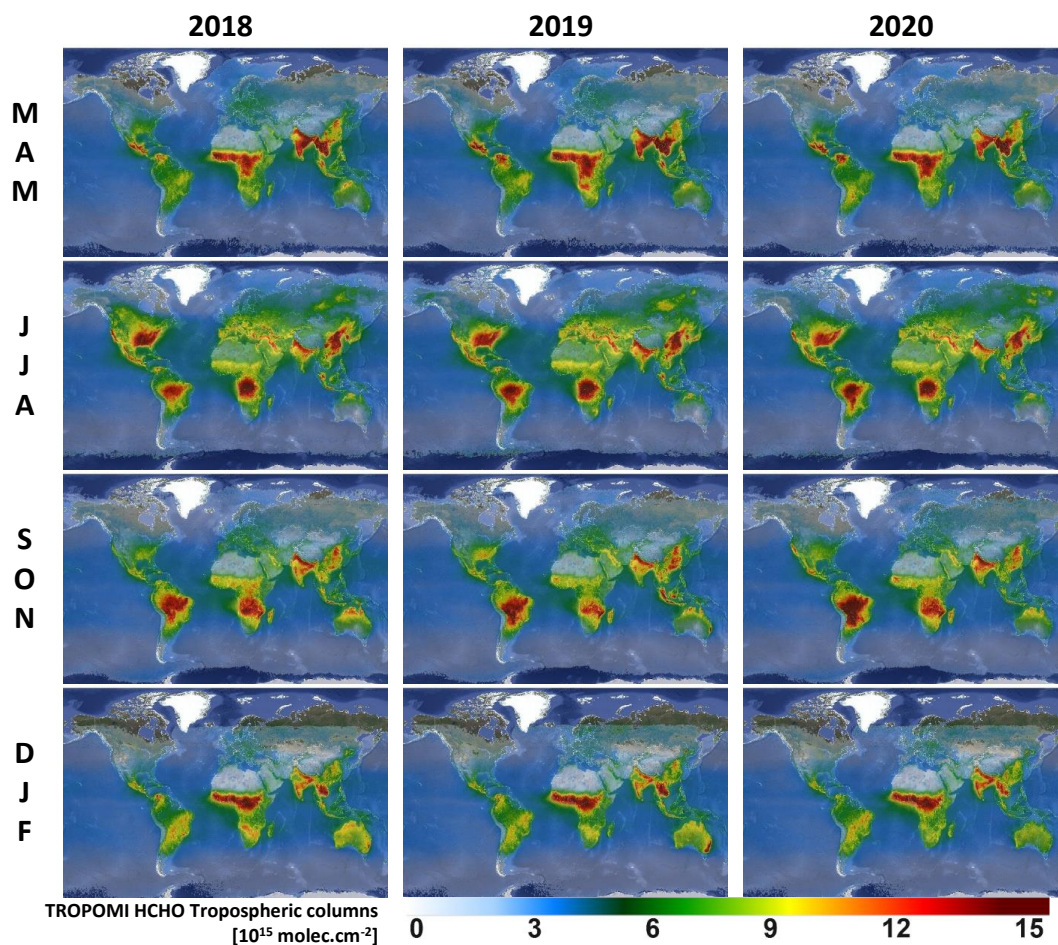
246 For the satellite/satellite and the satellite/ground-based comparisons, we calculate the median of the absolute
247 differences (absolute bias) and the median of the relative differences (relative bias) in each region or station (relative
248 either to TROPOMI in the case of sat./sat. or to the MAX-DOAS columns in the case of sat./ground-based). The
249 corresponding median absolute-value deviations (MAD) of the absolute and relative differences are a robust estimate
250 of the combined observation and comparison variability. The MAD is defined as the median of the absolute-value
251 deviations from the data's median:

$$MAD = k \cdot \text{median}(\text{abs}(\text{Diff}_i - \text{median}(\text{Diff}_i))) \quad (2-3)$$

252 where the factor $k=1.4826$ is used to ensure a correspondence with the 1-sigma standard deviation for normal
253 distribution. The bias is considered as statistically significant if it exceeds $\text{ErrB}=2 \cdot \text{MAD}/\sqrt{N}$, where N is the
254 number of collocated pairs (days or months). We also derive correlation, slope and offset of the linear regression using
255 the robust Teil-Shein estimator (Sen, 1968) as done in Vigouroux et al. (2020).



256 3 TROPOMI HCHO tropospheric columns



257 Figure 1: Seasonal maps of TROPOMI HCHO tropospheric columns during the three first years of measurements (March
258 2018 – February 2021), on a spatial grid of 0.05° in latitude and longitude. Observations are filtered using the $qa_values > 0.5$.
259 (max.scale: 15×10^{15} molec.cm $^{-2}$). Modified Copernicus Sentinel-5P satellite data, OFFL L2 HCHO product, BIRA-
260 IASB/DLR/ESA/EU.

261 As an illustration of the data product, Figure 1 displays the global seasonal distribution of tropospheric HCHO columns
262 derived from TROPOMI observations between March 2018 and February 2021. The overall seasonality of the HCHO
263 columns is largely driven by the emissions of NMVOCs from the vegetation and by the interannual variability of
264 surface temperatures and solar radiation. As can be seen, in South Eastern US for example, the seasonal amplitude is
265 very important and dominated by biogenic emissions during summertime. On top of biogenic emissions, wildfires
266 present a large variability. Since 2018, many fire events occurred worldwide and can be traced e.g. in HCHO columns
267 during summer 2018 and 2020 in Western US, or during summer 2019 in Siberia. After a decrease of about 10 years
268 (De Smedt et al., 2015), South America experienced two intense fire seasons in 2019 and 2020. The year 2020 was
269 also marked by the huge Australian and Californian wildfires, respectively, in January and October 2020, detectable

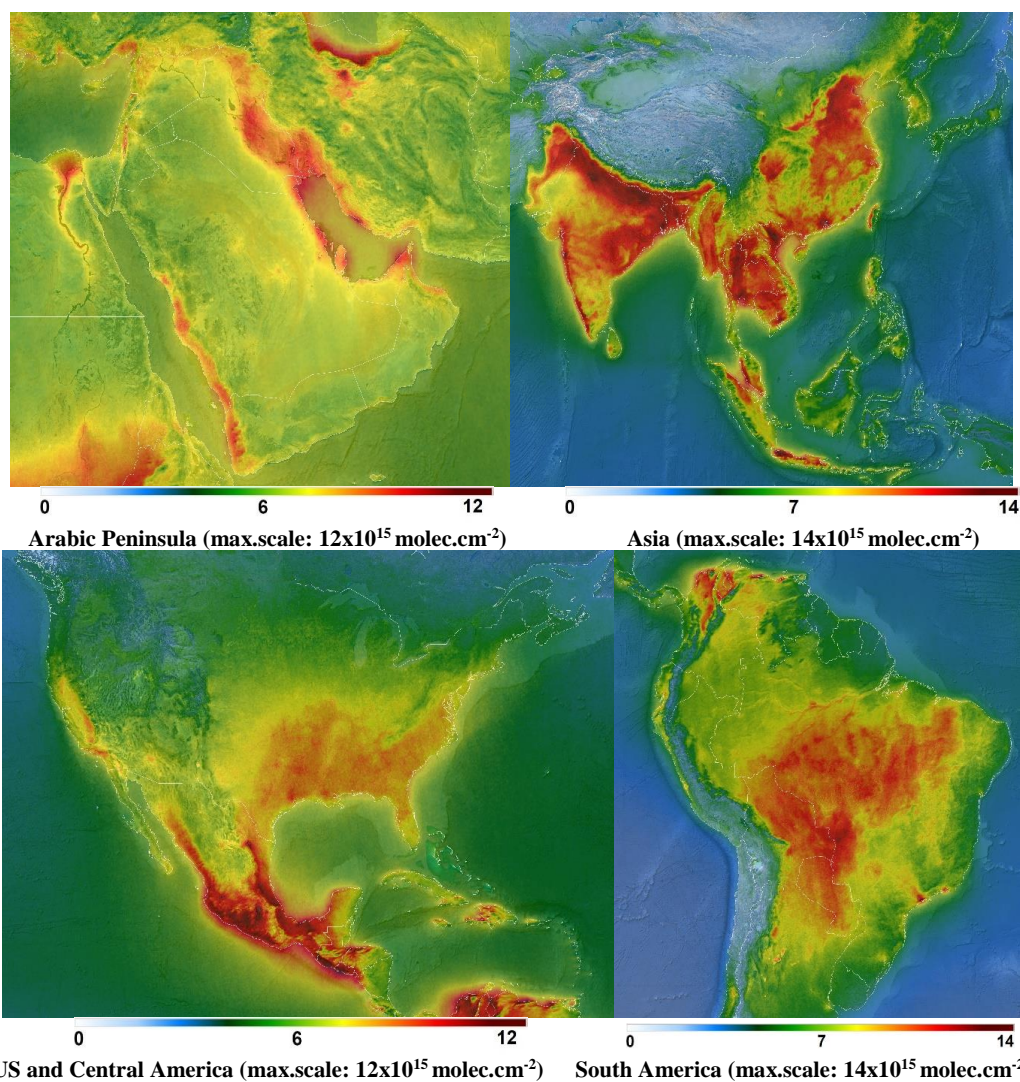


270 in the seasonal maps. In comparison to biogenic and pyrogenic emissions of natural origin, the contribution due to
271 anthropogenic NMVOC emissions to the total HCHO columns is generally lower. Although their oxidation is also
272 enhanced by sunlight, anthropogenic emissions show less seasonality than natural emissions, and their detection is
273 therefore generally easier in annual maps. This is illustrated in Figure 2, which presents 3-years averages of HCHO
274 columns over Asia, the Arabic Peninsula, the US and Central and South America, providing detailed information
275 about the spatial distribution of HCHO at the regional and urban scale. Europe and Africa are shown in the supplement
276 (fig.S1). Note that the colour scale has been adapted to the regions. Large urban areas are clearly visible in the HCHO
277 distribution in Asia, the Middle East and South America. With a lower magnitude, US cities are also clearly detectable,
278 such as Houston, Dallas or Los Angeles. HCHO levels are noticeably lower in Europe, but some urban areas are
279 visible in the Southern countries.

280 The quality of the TROPOMI observations also allows observing HCHO columns on a much shorter time scale with
281 an unprecedented definition. Daily observations of fire plumes are a clear step forward in the satellite remote sensing
282 of HCHO. They can be observed over much longer distances than before, thanks to the daily global coverage, coupled
283 with the finer spatial resolution and the improved signal to noise ratio, allowing to detect lower columns transported
284 further away (Alvarado et al. 2020; Theys et al. 2020). Not only wildfires, but also important anthropogenic emission
285 plumes can be observed on a daily basis, for example on the Eastern coast of Saudi Arabia. A few illustrations are
286 given in fig.S2. The TROPOMI performances for the observations of HCHO are discussed more quantitatively along
287 the paper in terms of precision and bias, as a function of the HCHO levels, and of the temporal and spatial scales.



288



289 Figure 2: Multi-annual regional maps of TROPOMI HCHO tropospheric columns (March 2018 – February 2021), on a
290 spatial grid of 0.05° in latitude and longitude. Observations are filtered using the $qa_values > 0.5$. Modified Copernicus
291 Sentinel-5P satellite data, OFFL L2 HCHO product, BIRA-IASB/DLR/ESA/EU.

292 4 Comparison between OMI and TROPOMI measurements

293 In this section, we evaluate the consistency between OMI and TROPOMI HCHO tropospheric columns. In addition,
294 we present the gain in precision obtained with TROPOMI. The analysis relies on 32 months of simultaneous
295 measurements from April 2018 to December 2020, allowing for a meaningful comparison at different scales. We first

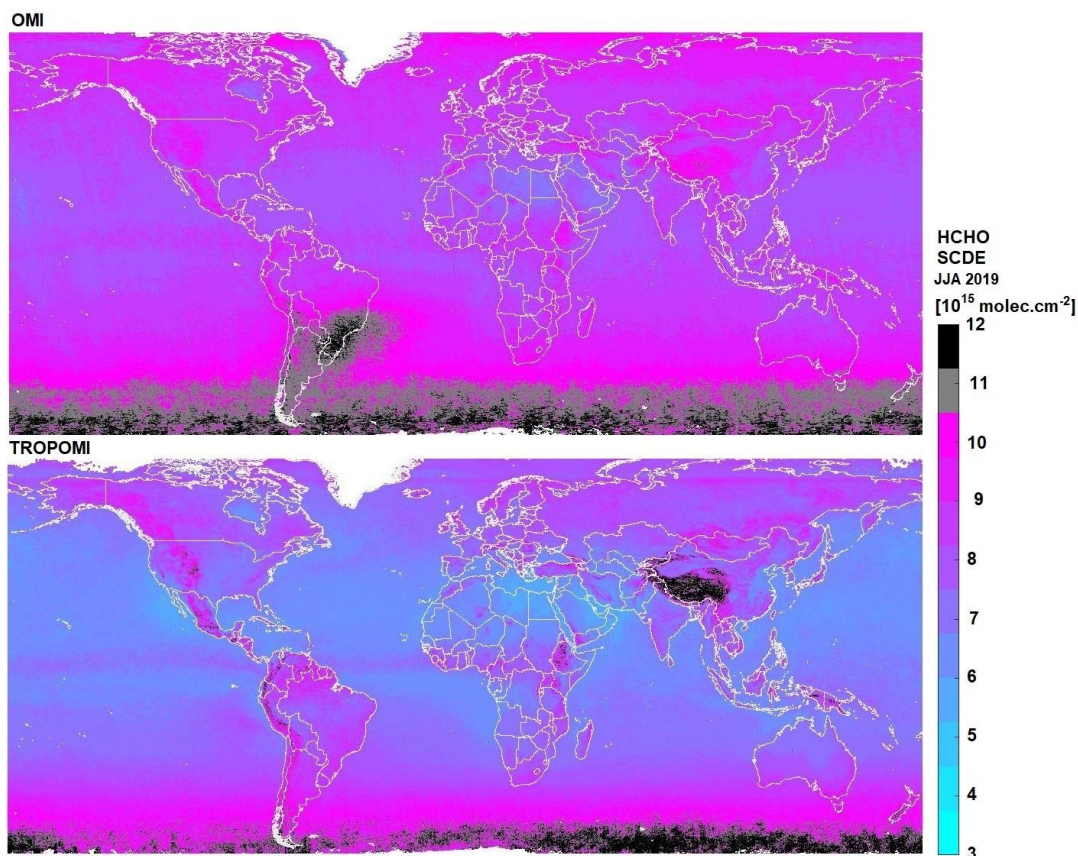


296 compare the precision obtained on individual measurements, and then proceed with a comparison of the precisions
297 achieved when averaging data at different spatial and temporal scales.

298 **4.1 HCHO slant column precision**

299 The random uncertainty of the tropospheric HCHO column is dominated by the error on the fitted slant column
300 densities (SCDE) which is directly related to the signal to noise ratio (SNR) of the measurement. From this point of
301 view, TROPOMI performs significantly better than previously launched nadir UV-VIS satellite instruments. In the
302 spectral range of HCHO retrievals (328.5-359 nm), the SNR of the TROPOMI spectra exceeds pre-flight requirements
303 that were based on OMI specifications (Kleipool et al., 2018; Ludewig et al., 2020).

304 Figure 3 presents global maps of SCDE averaged over 3 months during summer 2019, from OMI and TROPOMI.
305 From the improved SNR of TROPOMI in the UV range, TROPOMI HCHO SCDEs of individual observations are
306 about 25% lower than OMI ones. Over remote areas, the TROPOMI SCDE is about 6×10^{15} molec.cm⁻², while it is
307 8×10^{15} molec.cm⁻² for OMI. Slant column density errors are also improved over emission areas and at larger SZA.
308 Contrary to OMI, the effect of the South Atlantic Anomaly is absent in TROPOMI SCDE. This probably results from
309 a better shielding of the instrument against extra-terrestrial high energy radiation. The implemented iterative spike
310 algorithm (De Smedt et al., 2018) is also more efficient because of the lower noise level of the instrument. Note
311 however that over mountains, TROPOMI SCDE are higher than OMI ones. The most obvious effect is observed over
312 the Himalayans, but other chains such as the Andes or the Rocky mountains are also affected. This effect has been
313 identified as a scene inhomogeneity effect (Richter et al., 2018; 2020). The effect is also visible along the borders of
314 bright lakes or white surfaces. OMI retrievals are also affected by scene inhomogeneity effects, but the larger size of
315 the ground pixels and the larger mean SCDE values make its detection more difficult. We note that in the long-term
316 averaged maps of the HCHO tropospheric columns, some collocated artefacts appear (Figure 2, e.g. the white sands
317 in the US, Tuz Golu lake in Turkey or Lake Mackay in Australia). Most of the snow/ice scenes are eliminated by the
318 quality assurance values. The observations could however be better filtered over mountains and along the lake borders,
319 or even corrected during the fit of the slant columns as demonstrated for NO₂ and glyoxal (Lerot et al., 2021, in prep.).
320 The relatively coarse albedo climatology also needs to be updated with a TROPOMI-based product, better defined in
321 space and time (Loyola et al., 2020).



322

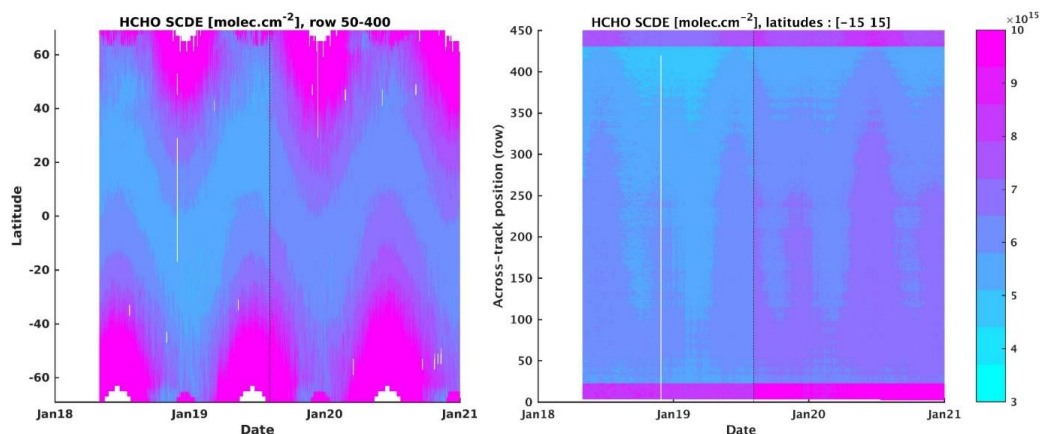
323 **Figure 3: Average HCHO slant column density fitting error (SCDE) retrieved from OMI (upper panel) and TROPOMI**
324 **(lower panel) in JJA 2019, on a spatial grid of 0.05° in latitude and longitude.**

325 The OMI SCDEs have been very stable over the years, showing a limited increase of about 5% between 2005 and
326 2019 (De Smedt et al., 2018). However, the number of valid OMI observations has decreased by about 30% during
327 the same period (-50% at large SZA) due to the row anomaly. In order to evaluate the stability of the TROPOMI
328 HCHO retrievals during the three first years, Figure 4 presents the time series of the TROPOMI HCHO slant column
329 errors in the remote Pacific Ocean as a function of latitude and instrumental rows. As expected, we observe an increase
330 of the noise for large SZAs, and for the 25 first and last rows of the scan, which have a different detector binning ([L1b](#)
331 [ATBD](#)). The fact that the algorithm makes use of daily updated radiances as reference for the DOAS fit allows for
332 very stable results in time and across the rows. Only the change in pixel size in August 2019 ([L1b readme file](#)) resulted
333 in a moderate step increase of the SCDE of about 15%. These values are compared to the observed standard deviation
334 of the slant columns in the same regions (see fig.S3). We observe a very good agreement between the SCDEs and the
335 standard deviation, indicating that they give a good representation of the random errors.

336 The reported uncertainty on the tropospheric vertical columns due to random errors corresponds to the SCDE divided
337 by the AMF for each observation. In the Equatorial Pacific, the TROPOMI vertical column precision is about 5×10^{15}



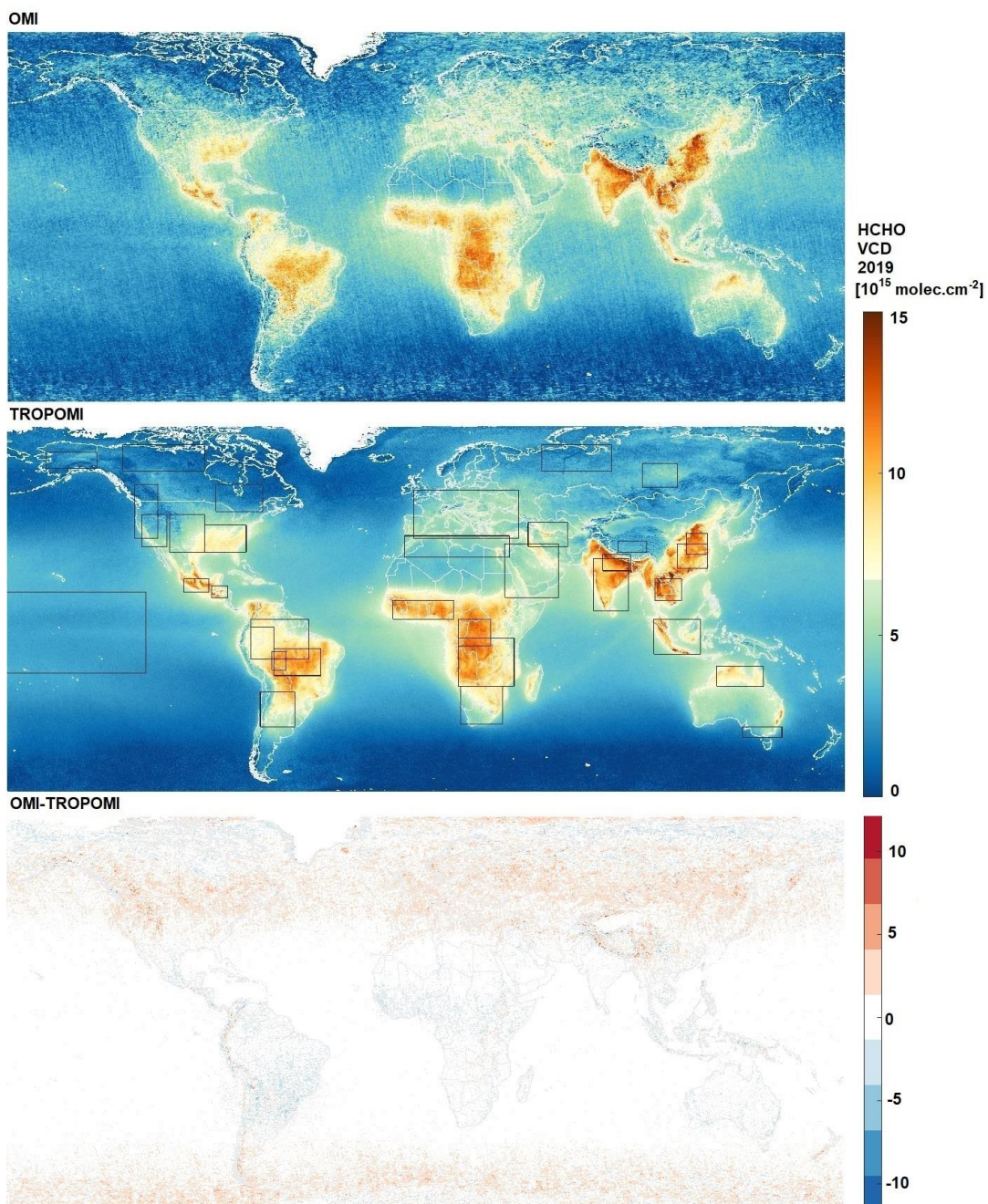
338 molec.cm⁻², while it is 7x10¹⁵ molec.cm⁻² for OMI. It is larger over continental emissions, where the AMFs are
339 generally smaller than 1.



340 **Figure 4: TROPOMI HCHO slant column density errors (SCDE) as a function of the latitude (left column) or the detector**
341 **row (right column). The step increase on 6th August 2019 reflects the change in the TROPOMI pixel size (indicated with**
342 **the black line).**

343 4.2 HCHO tropospheric columns

344 Figure 5 presents the yearly averaged OMI and TROPOMI HCHO vertical columns (N_{v_clear}) for 2019. Even at this
345 level of averaging, the lower noise level of TROPOMI is very clear, especially for low to medium HCHO levels. We
346 observe an overall good agreement of the columns both in magnitude and in their spatial distribution. Differences of
347 TROPOMI and OMI yearly averages range from +2x10¹⁵ molec.cm⁻² over Tropics to -2x10¹⁵ molec.cm⁻² over mid-
348 latitude regions. Differences tend to increase with latitudes. However, as the quality of the TROPOMI observations is
349 improved at large solar zenith angles, more data in winter months are kept in the TROPOMI dataset, which can
350 influence yearly averaged columns at those latitudes. In order to provide quantitative comparisons, we calculated daily
351 and monthly averaged columns in 35 regions covering a broad range of emission levels and observation conditions
352 (large black boxes on Figure 5). As the regions are large, many observations are included (on average 500/day for
353 OMI, 12500/day for TROPOMI). To obtain daily and monthly comparison pairs, we keep coincident days of
354 observations and follow the methodology presented in sect. 2.5.

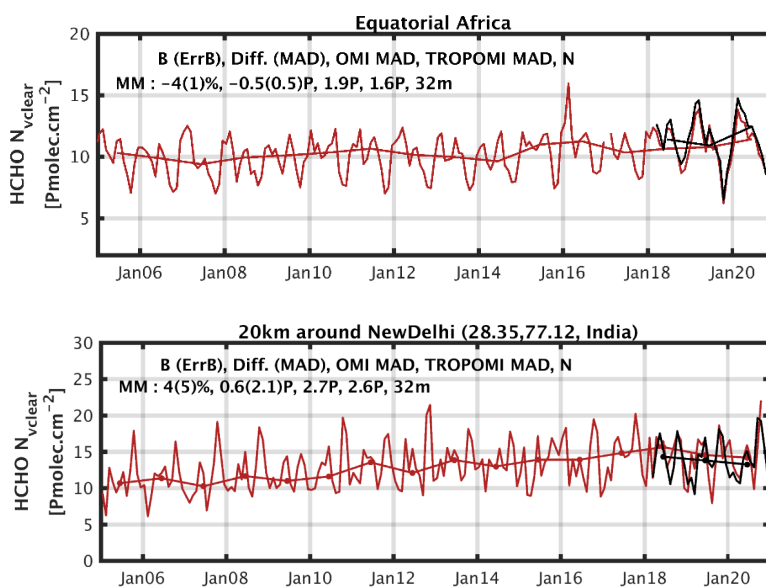


355

356 Figure 5: Average HCHO tropospheric column ($N_{v,clear}$) retrieved from OMI (first line) and TROPOMI (second line) in
357 2019. Limits of the regions selected for the comparisons are shown on the TROPOMI map. Differences between OMI and
358 TROPOMI maps are shown on the last panel. The same grid is used for both dataset (0.05°). Data are filtered using the
359 product quality flags. The large black boxes on the TROPOMI maps represent the regions used in the comparisons (see
360 Figure 6 and Figure 7).



361 An example of a time series over Equatorial Africa is presented on the first panel of Figure 6, where monthly averaged
362 $N_{v,clear}$ are shown, and comparison numbers are provided in the inset. In the Equatorial African region, the seasonal
363 cycle is marked by two peaks during the dry seasons and two minima during the wet seasons. In 2019, the minimum
364 was particularly low, observed in both the OMI and TROPOMI timeseries, while the maxima tend to increase over
365 the years. More examples of time series can be found in fig.S4. In all the regions, the seasonal and interannual
366 variability of the HCHO columns are observed very consistently with OMI and TROPOMI.



367 **Figure 6: Examples of monthly and yearly averaged HCHO columns ($N_{v,clear}$) retrieved from OMI (Oct.2004-Dec.2020, in**
368 **red) and TROPOMI (2018-Dec.2020, in black) at two different spatial scales selected for the comparison: a large region of**
369 **Equatorial Africa, and a circle of 20km-radius over New Delhi in India. Absolute and relative biases between OMI and**
370 **TROPOMI HCHO monthly averaged columns are given in inset, as well as the median deviations of the OMI and**
371 **TROPOMI averaged columns. [$\text{Pmolec.cm}^{-2} = 1 \times 10^{15} \text{ molec.cm}^{-2}$].**

372 Figure 7 presents the absolute and relative biases between OMI and TROPOMI HCHO tropospheric columns for all
373 regions. Numbers are provided for daily averaged columns applying a cloud correction (N_v) or not ($N_{v,clear}$). Regions
374 are sorted as a function of the averaged TROPOMI HCHO column. At this large spatial scale, the regions over
375 Equatorial Africa, Northern China and Northern India present the largest annual columns worldwide, with median
376 levels larger than $10 \times 10^{15} \text{ molec.cm}^{-2}$. Tropical regions in South America, Africa and Asia present elevated levels of
377 HCHO as well, with annual averaged columns larger than $8 \times 10^{15} \text{ molec.cm}^{-2}$.

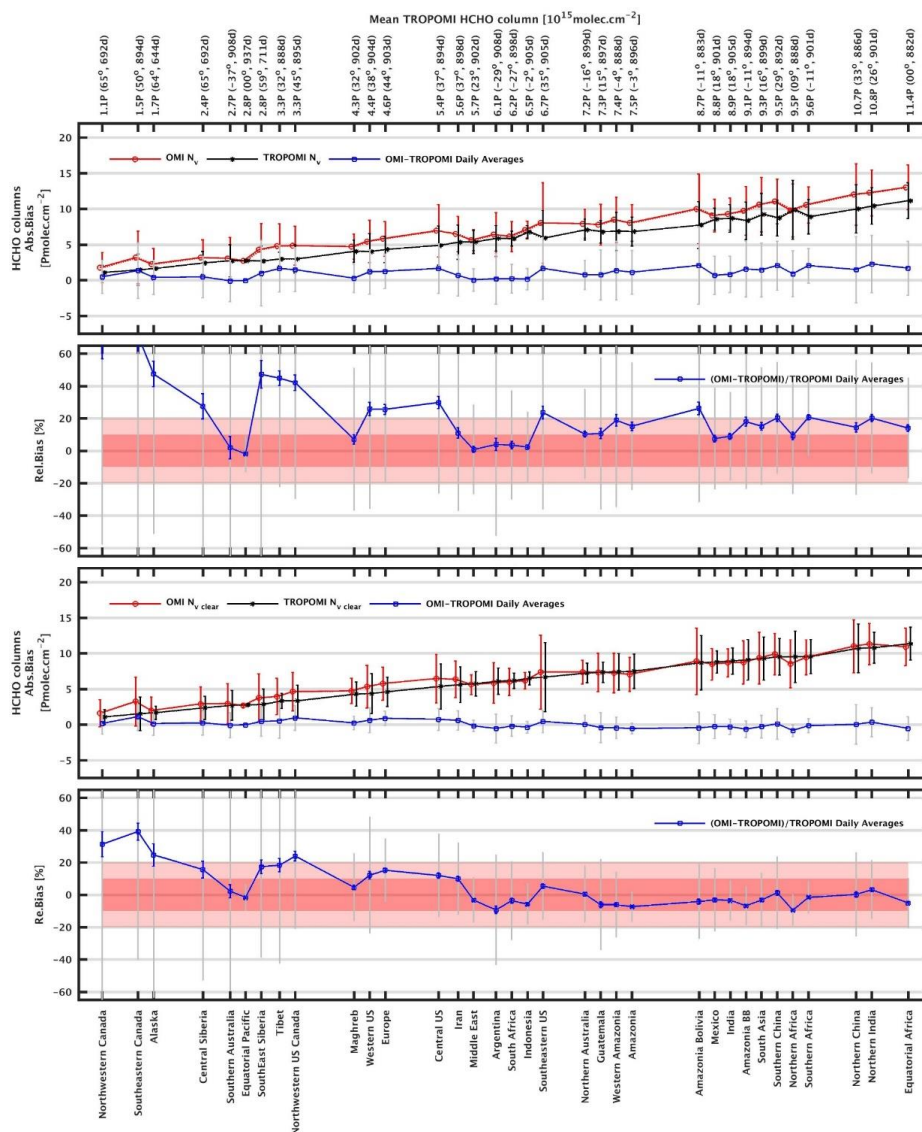
378 Looking at N_v comparisons, it appears that the OMI HCHO columns present a positive bias compared to TROPOMI
379 from $17 \pm 2.5\%$ for the columns larger than $5 \times 10^{15} \text{ molec.cm}^{-2}$, to $30 \pm 5\%$ for the lower columns. This bias exceeds
380 50% in Northern latitudes ($>45^\circ$) and low-emissions ($<2 \times 10^{15} \text{ molec.cm}^{-2}$) regions of Canada and Alaska. However,
381 when comparing $N_{v,clear}$, the biases are strongly reduced below 10% in all regions where the HCHO levels are larger
382 than $5 \times 10^{15} \text{ molec.cm}^{-2}$, and the TROPOMI columns are found to be slightly larger than OMI on average ($-3 \pm 1.2\%$).
383 In mid-Northern-latitudes/moderate emissions ($2-5 \times 10^{15} \text{ molec.cm}^{-2}$) regions such as Europe, Central and Western



384 US, North Western Canada, Siberia or Tibet, OMI columns present a remaining bias of about $15\pm 3\%$, while in the
385 regions of Canada and Alaska, a larger bias of about $+30\pm 7\%$ remains. Note that we observe biases lower than 10%
386 in the Maghreb and Southern Australia regions, despite their relatively low columns or low latitudes.
387 We conclude that biases up to 30% related to the cloud correction are observed over Tropical regions where the clouds
388 are the highest in altitude (Africa, South America, South Asia), and a smaller but systematic effect, up to 15%, is
389 observed over mid-latitude polluted regions such as China, India, US or Europe. We also note that the differences
390 between N_v and N_{v_clear} are mainly significant for the OMI HCHO columns. It has been reported that the cloud
391 pressures retrieved from TROPOMI and from OMI present a bias (OMI clouds are higher in altitude, Compernelle et
392 al., 2020). This translates into OMI cloud-corrected air mass factors generally smaller than TROPOMI AMFs by 5 to
393 30%, depending on the cloud altitude, and therefore in a positive bias of the OMI HCHO VCD compared to the
394 TROPOMI product. It is therefore important to keep in mind that the use of different cloud products may introduce
395 inconsistencies, which may be resolved by using clear HCHO VCDs (N_{v_clear}).
396 Figure 8 shows the linear regression between OMI and TROPOMI monthly averaged columns, considering all regions
397 together. The relation between OMI and TROPOMI is provided for N_v and N_{v_clear} . This shows that switching off the
398 cloud correction in the OMI and TROPOMI HCHO products allows to significantly improve not only the slope (from
399 0.87 to 0.92) and the intercept (from 1.52 to 0.48×10^{15} molec.cm⁻²), but also the data scatter, i.e. the Pearson R
400 correlation (from 0.74 to 0.98). When considering large-scale comparisons, the agreement between OMI and
401 TROPOMI N_{v_clear} is therefore very satisfactory.



402



403

404

405

406

407

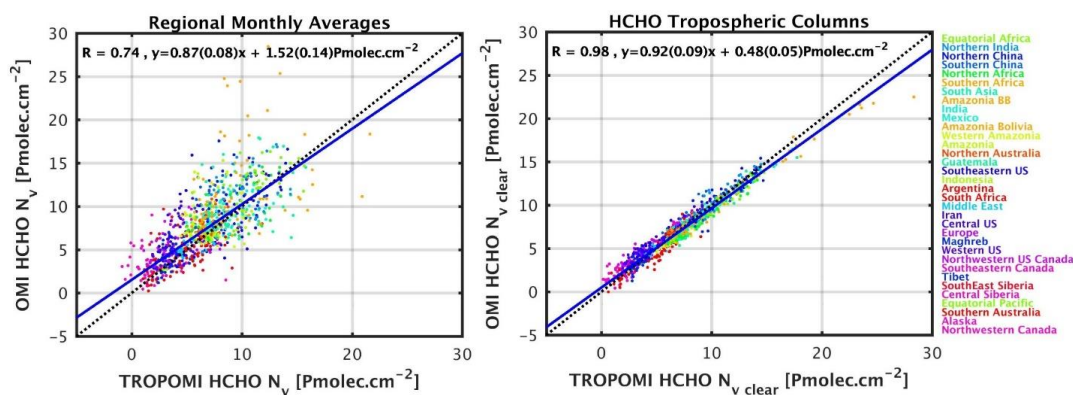
408

409

Figure 7: Absolute and relative biases between OMI and TROPOMI HCHO daily averaged tropospheric columns using cloud corrected AMF (N_v , two upper panels) or clear sky AMF ($N_{v,clear}$, two bottom panels) for the large regions represented on Figure 5. Regions are sorted as a function of the median TROPOMI HCHO column. Values of the averaged HCHO columns are provided on the top axis, as well as the numbers of common days taken for the comparison and the latitude of the region. The median OMI (red) and TROPOMI (black) columns are plotted together with the absolute differences (in blue). Error bars represent the median deviations of the columns, or the median absolute deviations of



410 differences (MAD, in grey). Statistical ErrB are also plotted for the relative bias (in blue). Pink areas indicate 10% and
411 20% bias. [$\text{Pmolec.cm}^{-2} = 1 \times 10^{15} \text{ molec.cm}^{-2}$].



412

413 **Figure 8: Scatter plots of OMI versus TROPOMI columns for the monthly means of collocated data. Results are shown for**
414 **N_v (left panel) and $N_{v,clear}$ (right panel). The correlation, slope and intercept of a linear regression using the robust Teil-**
415 **Shein estimator are given as inset and plotted as a blue line. Black dotted line is the 1:1 line. The color indicates the latitude**
416 **of the region. [$\text{Pmolec.cm}^{-2} = 1 \times 10^{15} \text{ molec.cm}^{-2}$].**

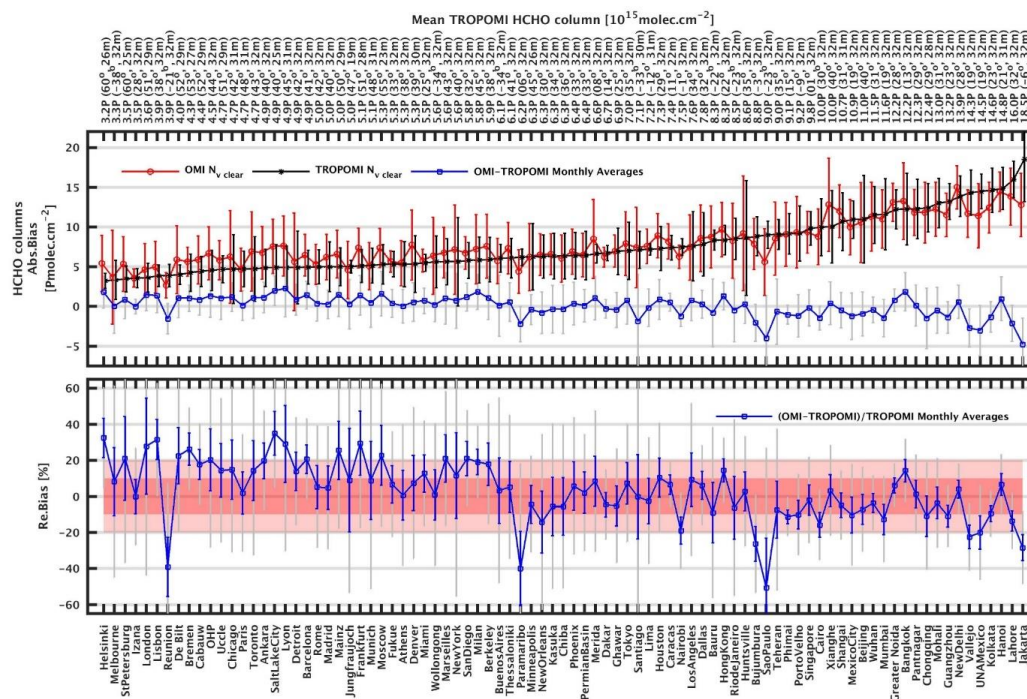
417 When averaging data over large regions, the dispersion due to random uncertainties is greatly reduced compared to
418 individual observations. As summarized in Table 2, the median absolute deviations of the monthly averaged columns
419 are equivalent for OMI and TROPOMI ($1.8 \times 10^{15} \text{ molec.cm}^{-2}$), while the MAD of their differences are significantly
420 lower ($0.5 \times 10^{15} \text{ molec.cm}^{-2}$). This indicates that at this spatiotemporal resolution, the natural variability dominates the
421 dispersion of the averaged observations. Looking at the daily averaged columns, the TROPOMI median deviation is
422 lower than for OMI (2.2/2.7), but still larger than the MAD of their differences (1.5).

423 The improved spatial resolution of TROPOMI should allow for a better detection of localized HCHO emissions. To
424 address this question, we performed the same comparisons as for the large regions, but looking at smaller areas of
425 20km radius around cities. Figure 9 presents the absolute and relative biases of the monthly averaged HCHO columns
426 ($N_{v,clear}$) for a large number of cities. At this spatial scale, Jakarta is the location with the largest median HCHO level
427 ($>18 \times 10^{15} \text{ molec.cm}^{-2}$ over the 2018-2020 period). Indian, Chinese and other Asian cities follow, as well as Mexico,
428 Monterrey or Kinshasa ($>12 \times 10^{15} \text{ molec.cm}^{-2}$). Sao Paulo, Tehran and Cairo present also noticeably elevated HCHO
429 levels ($>9 \times 10^{15} \text{ molec.cm}^{-2}$). An example over New Delhi is presented on the second panel of Figure 6 and more
430 examples can be found in fig.S5.

431 When comparing OMI and TROPOMI $N_{v,clear}$ around the cities, the same general behaviour as in the large regions
432 can be observed. OMI presents a positive bias ($20 \pm 15\%$) compared to TROPOMI for low to medium HCHO levels,
433 while for medium to large levels, the agreement is very good on average ($-1 \pm 10\%$). There are nevertheless a few
434 exceptions where TROPOMI HCHO columns are significantly larger than the OMI ones. This is the case at La
435 Reunion, Paramaribo, Nairobi, Bujumbura, Sao Paulo, Monterrey, Mexico, or Jakarta. Those cities are located along
436 marine coasts or lakes, at higher altitude, or are surrounded by mountains. In those cases, the finer spatial resolution
437 of TROPOMI clearly improves the detection of the HCHO signal. For most other locations, however, the impact of
438 the improved spatial resolution of TROPOMI on the HCHO columns is not detectable in the column magnitudes,



439 when compared to OMI observations. This is likely related to the nature of the HCHO production that mostly is
 440 secondary from the oxidation of NMVOCs with various lifetimes (Stavrakou et al. 2015; Bauwens et al., 2016). Except
 441 for regions where the topography presents sharp discontinuities, this causes a natural spread of the HCHO columns at
 442 a scale larger than the TROPOMI spatial resolution.
 443 Note however that at this spatial resolution (20km radius), the level of noise is larger than for the regional averages
 444 and the TROPOMI averaged columns are significantly more stable than the OMI ones, as evidenced by their median
 445 deviations (see). On a daily basis, the OMI columns present a dispersion of 7.8×10^{15} molec.cm⁻², while the TROPOMI
 446 dispersion is about twice smaller (3.7×10^{15} molec.cm⁻²). In this case, the MAD of the differences (7.1×10^{15} molec.cm⁻²)
 447 is dominated by the noise on OMI observations. Note that these estimates still include the natural variability of the
 448 columns themselves. If an area of 20-km in the remote Equatorial Pacific is considered, the observations represent
 449 constant background values and the seasonal variability is further reduced. In such conditions, the dispersion of the
 450 OMI daily observations is 3.5×10^{15} molec.cm⁻², while only 1×10^{15} molec.cm⁻² for TROPOMI. We show in the next
 451 section that validation with ground-based measurements brings further information on the satellite column precision.



452
 453 **Figure 9: Absolute and relative biases between OMI and TROPOMI HCHO monthly averaged tropospheric columns using**
 454 **clear sky AMF ($N_{v,clear}$) within 20km-radius circles around selected cities, sorted as a function of the median TROPOMI**
 455 **HCHO column. Value of the averaged HCHO columns are provided on the top axis, as well as the numbers of months taken**
 456 **for the comparison, and the latitude of the region. The median OMI (red) and TROPOMI (black) columns are plotted**
 457 **together with the absolute differences (in blue). Error bars represent the median absolute deviations (MAD) of the columns**
 458 **and of the differences (in grey). Statistical ErrB are also plotted for the relative bias (in blue). Pink areas indicate 10% and**
 459 **20% bias. [Pmolec.cm⁻² = 1×10^{15} molec.cm⁻²].**



460 **Table 2: Median absolute deviation of the OMI and TROPOMI daily and monthly averaged columns ($N_{v,clear}$), in large**
461 **regions and in 20km-radius area. MAD of differences between OMI and TROPOMI columns are also given in the last**
462 **column.**

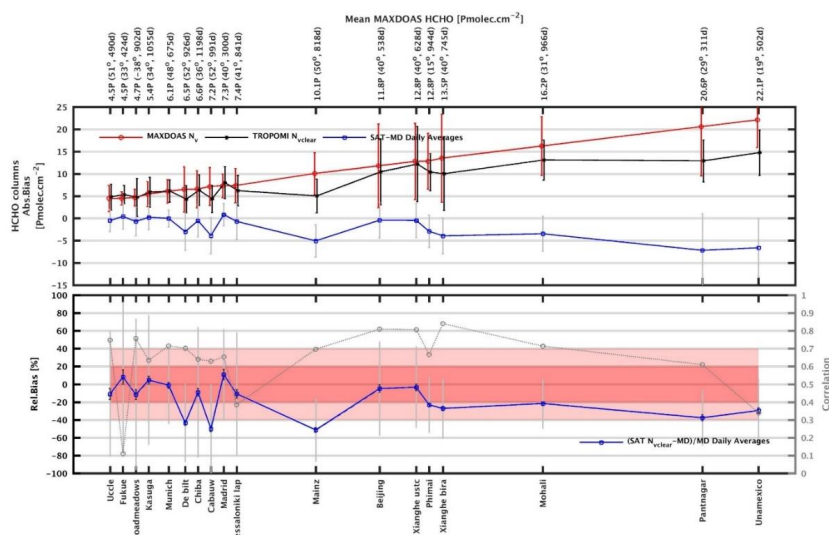
Dispersion	OMI MAD [10^{15} molec.cm $^{-2}$]	TROPOMI MAD [10^{15} molec.cm $^{-2}$]	OMI-TROPOMI MAD [10^{15} molec.cm $^{-2}$]
Monthly Regional	1.8	1.8	0.5
Daily Regional	2.7	2.2	1.6
Monthly 20km	3.3	2.5	2.4
Daily 20km	7.8	3.7	7.1
Daily 20km in the Equatorial Pacific	3.5	1.0	3.7

463 5 Validation with a global MAX-DOAS network

464 Here, we present a validation exercise based on a network of 18 ground-based MAX-DOAS instruments. This effort
465 complements the study of Vigouroux et al. (2020), which relied on a network of FTIR instruments. Compared to the
466 FTIR instruments, the MAX-DOAS provide a higher sensitivity in the boundary layer, where the bulk of HCHO is
467 located. The MAX-DOAS network covers stations where the level of HCHO is significant, from medium to very large
468 HCHO columns, while the FTIR network includes a larger number of remote stations. In this study, we validate in
469 parallel the OMI and TROPOMI datasets. We first focus on a direct comparison of the satellite and MAX-DOAS
470 tropospheric columns. The effect of the vertical smoothing is investigated in the next subsection for three stations.

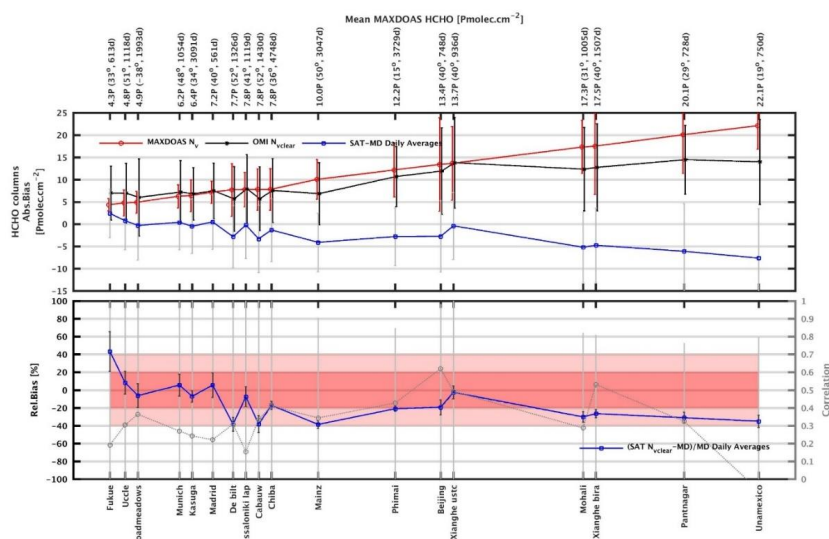
471 5.1 Direct comparisons of tropospheric columns

472 For each station in Table 1, we consider daily averages of the satellite columns in a radius of 20km around the
473 instruments. We average MAX-DOAS columns between 11h and 16h local time. We keep coincident days of
474 observations (OMI/MAX-DOAS, TROPOMI/MAX-DOAS) to obtain daily and monthly comparison pairs. Note that
475 the time periods used for the comparison are not the same for OMI and TROPOMI, and vary between the stations. To
476 obtain the validation results, we follow the methodology presented in Vigouroux et al. (2020) (see sect. 2.5).



477

478 **Figure 10: Absolute (top, blue line) and relative biases (bottom) between MAX-DOAS and TROPOMI HCHO daily**
 479 **averaged tropospheric columns in a circle of 20km-radius around the stations. Regions are sorted as a function of the**
 480 **median MAX-DOAS HCHO column. In the upper plot, the median MAX-DOAS (red) and TROPOMI (black) columns are**
 481 **plotted together with the differences. Error bars (in grey) represent the median absolute deviations (MAD) of the columns**
 482 **and of the differences. Statistical ErrB are also plotted for the relative bias (in blue). Pink areas indicate 20% and 40%**
 483 **bias. The correlation between the daily observations are given in the lower plot (grey circles). [Pmolec.cm⁻² = 1x10¹⁵**
 484 **molec.cm⁻²].**



485

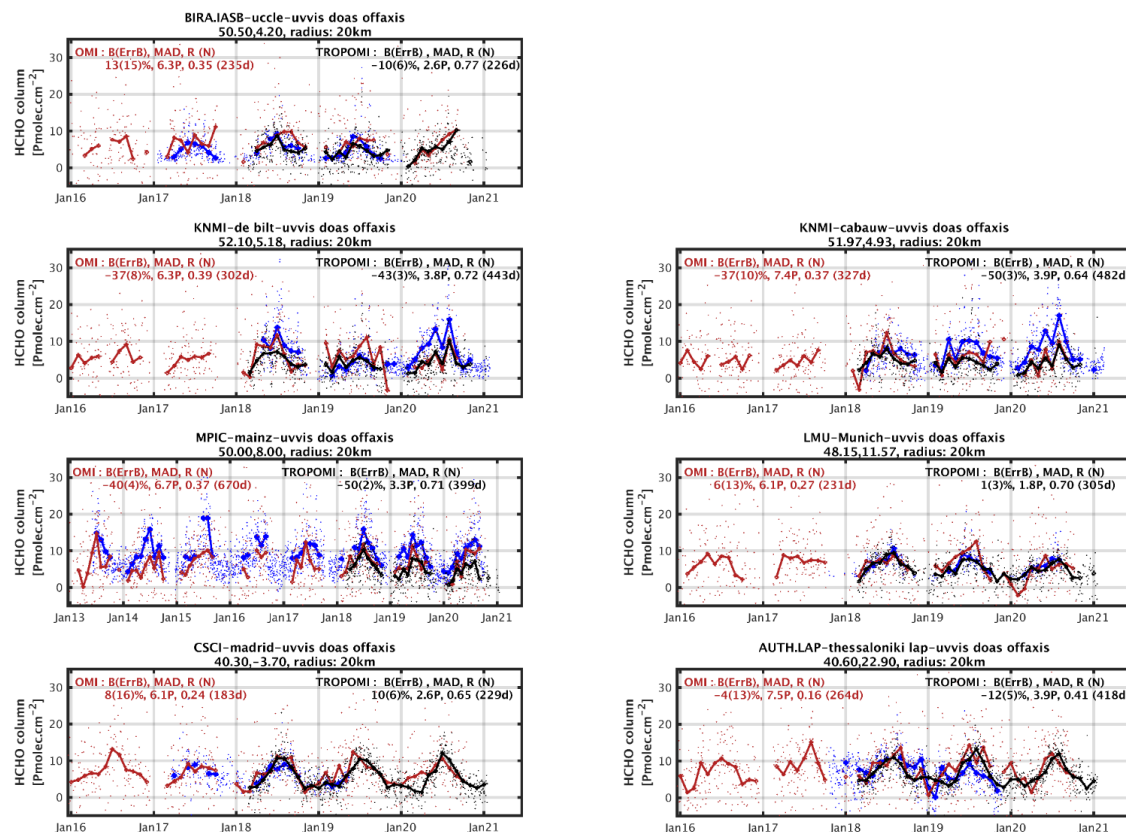
486 **Figure 11: same as Figure 10 for MAX-DOAS and OMI HCHO daily averaged.**

487



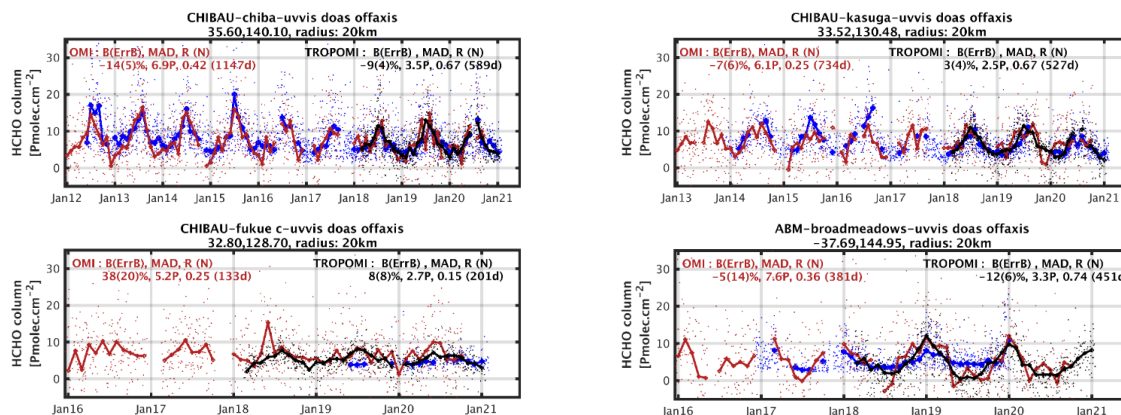
488 Figure 10 and Figure 11 present the absolute and relative biases of the daily averaged columns as a function of the
489 median MAX-DOAS HCHO column, respectively, for TROPOMI and OMI. A more detailed description for each
490 station and for individual time series is presented afterwards. The values of the biases are similar for OMI and
491 TROPOMI, except for the lowest columns in Uccle and Fukue, where OMI presents larger positive biases exceeding
492 +20%. In agreement with Vigouroux et al. (2020), TROPOMI columns do not present a significant bias for the range
493 of HCHO levels from 4 to 8×10^{15} molec.cm⁻². Note that, in contrast to FTIR data, the range of values covered by our
494 MAX-DOAS network does not extend to columns lower than 4×10^{15} molec.cm⁻². We observe that the stations in De
495 Bilt and Cabauw tend to show somewhat stronger negative biases even for medium levels of HCHO, which might
496 point to a network inhomogeneity. For larger HCHO columns ($> 8 \times 10^{15}$ molec.cm⁻²), and in agreement with the FTIR
497 results, we observe that negative biases tend to increase for large HCHO columns such that the underestimation of the
498 satellite columns reaches about -40% for the largest columns. On the upper plot, the error bars represent the median
499 absolute deviations of the columns and of their differences. It appears clearly that the MADs obtained with TROPOMI
500 are substantially lower than those obtained with OMI. Note that the type of MAX-DOAS instrument (in particular its
501 signal-to-noise ratio) may also influence the observed MAD at the different stations.

502 Figure 12, Figure 13 and Figure 14 present more detailed results for the stations in Europe, Japan and Australia, and
503 China, India, Thailand and Mexico. On each plot, the time series of the MAX-DOAS, OMI and TROPOMI data are
504 displayed together. Results of the daily statistical analysis are given as inset. At European stations, which show
505 medium range HCHO levels, we obtain contrasted results. With a mean HCHO column of 4.5×10^{15} molec.cm⁻², Uccle
506 is one of the stations with the lowest columns of the network presented in this paper. While OMI values show a
507 positive bias ($13 \pm 15\%$) and a poor correlation (0.3) with the MAX-DOAS, TROPOMI appears to be biased low ($-$
508 $10 \pm 6\%$) but much better correlated (0.82) with the MAX-DOAS data. As opposed to Uccle, the observed biases in De
509 Bilt, Cabauw, and Mainz are largely negative (from -40% to -50%). The correlations found with TROPOMI are
510 nevertheless much better than with OMI. Note that the median MAX-DOAS HCHO value in Mainz is larger than
511 10×10^{15} molec.cm⁻², which is quite high for an European site. The results in Munich have been presented in details in
512 Chan et al. (2020). They are closer to what is found in Uccle, with a small positive bias for TROPOMI ($1 \pm 3\%$) and
513 for OMI ($6 \pm 13\%$). Similarly in Madrid, OMI and TROPOMI results are very consistent with a mean bias of
514 respectively $8 \pm 16\%$ and $10 \pm 6\%$. In Thessaloniki, the negative bias is $-12 \pm 5\%$, but the correlation is poorer than in
515 Madrid.



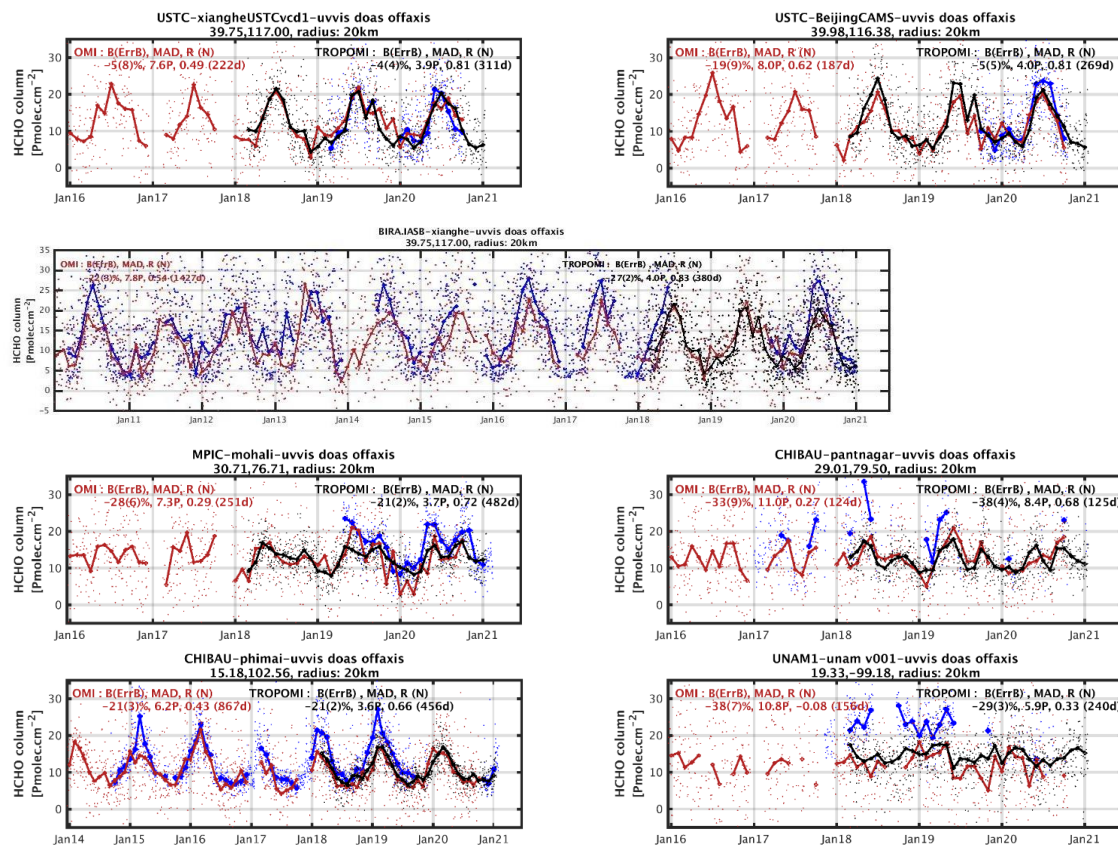
516 **Figure 12: Time series of MAX-DOAS HCHO columns (blue), OMI $N_{v,clear}$ (red) and TROPOMI $N_{v,clear}$ (black) at**
 517 **European sites. Thick lines show monthly median values and dots represent daily median values. Mean relative bias, median**
 518 **absolute deviations and correlations between the time series are provided for the daily averaged data. [$\text{Pmolec.cm}^{-2}=10^{15}$**
 519 **molec.cm^{-2}].**

520 In Figure 13, we show three Japanese stations operated by the CHIBA University. Mean HCHO levels in Japan are
 521 comparable to values found at European sites. In Chiba and Kasuga, TROPOMI and MAX-DOAS columns are
 522 strongly correlated (about 0.7), but on the island of Fukue the correlation is poor due to a lack of variability at this
 523 site. At all these sites, TROPOMI shows small biases compared to MAX-DOAS data ($-9\pm 4\%$ in Chiba, $3\pm 4\%$ in
 524 Kasuga, $8\pm 8\%$ in Fukue). The HCHO observations in Broadmeadows, in Northern Melbourne, have been published
 525 by Ryan et al. (2020). We find a bias of $-12\pm 6\%$ for TROPOMI and a good correlation of about 0.7. Quite unusually,
 526 the seasonal amplitude of the MAX-DOAS time series at this station is smaller than observed with OMI and
 527 TROPOMI.



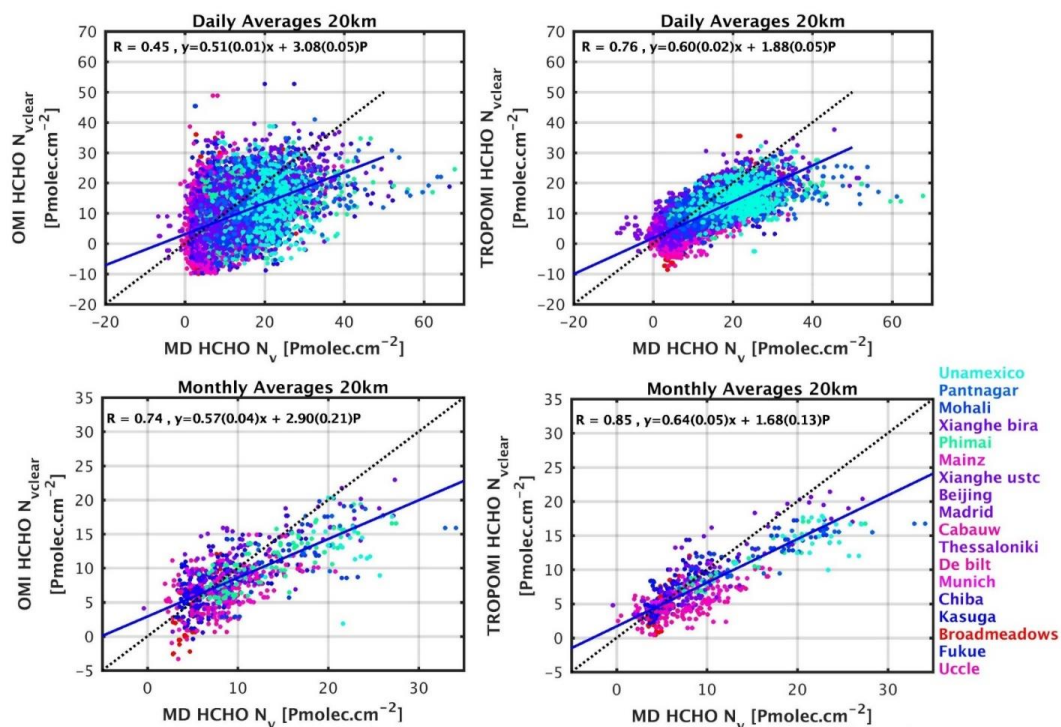
528 **Figure 13: Same as Figure 12 in Japan and Australia.**

529 Stations with large HCHO levels in China, India, Thailand and Mexico are presented in Figure 14. In China, we show
530 the results of two instruments in Xianghe, and one instrument in Beijing. With the USTC instruments, we find small
531 biases of $-4\pm 4\%$ and $-5\pm 5\%$ and correlations larger than 0.8. With the BIRA-IASB instrument in Xianghe, the
532 correlation is also excellent. The MAX-DOAS columns are larger than the ones obtained with the USTC instrument,
533 and we find a significant negative bias of the TROPOMI data of $-27\pm 2\%$. This result illustrates the actual uncertainty
534 related to the ground-based measurements themselves and the need for further harmonisation of the MAX-DOAS
535 network. Correlations in India and Thailand are of about 0.7, while the biases are consistently negative ($-21\pm 2\%$ in
536 Mohali, $-38\pm 4\%$ in Pantnagar, $-21\pm 2\%$ in Phimae). The situation is more complex at the UNAM site in Mexico. There,
537 the correlation is poor (0.3), and a negative bias of $-29\pm 3\%$ is found. These results are however more dependent on
538 the radius considered around the station, and on the selection of the MAX-DOAS observations (Rivera Cárdenas et
539 al., 2021) (see sect. 5.4).



540 **Figure 14: Same as Figure 12 at Chinese, Indian, Thailand and Mexican sites.**

541 Finally, Figure 15 presents scatter plots of the satellite against MAX-DOAS columns, considering all the stations and
 542 for daily and monthly comparisons. Table 3 summarizes the validation results. The best agreement is found with
 543 monthly TROPOMI columns, for which we find a slope of 0.64 and a positive offset of 1.7×10^{15} molec. cm^{-2} compared
 544 to the MAX-DOAS columns. Slopes and biases for the large columns are found to be close for OMI and TROPOMI
 545 datasets. The improvement with TROPOMI can be seen in the correlation, offset, and bias values obtained for the
 546 lower columns, as well as in the precision of the daily validation results. On average, the OMI biases are found to be
 547 statistically non-significant for the lowest columns. When considering monthly averaged data, the correlation between
 548 MAX-DOAS and satellite columns improves from 0.74 with OMI to 0.85 with TROPOMI (+15%). More importantly,
 549 it improves from 0.45 to 0.76 when considering daily observations (+68%). The daily offset is reduced by 60% from
 550 OMI to TROPOMI (3.1 to 1.9×10^{15} molec. cm^{-2}). In low-emission conditions, the MADs of the differences provide an
 551 upper limit of the precision of the satellite measurements. If we consider HCHO levels below 8×10^{15} molec. cm^{-2}
 552 (medium level, but the low range is not represented here), the precision of the daily TROPOMI HCHO observations
 553 is estimated to be 3×10^{15} molec. cm^{-2} , which represents an improvement of more than a factor 2 compared to OMI. The
 554 precision of monthly TROPOMI observations reaches 1.4×10^{15} molec. cm^{-2} , which is close to the Copernicus user
 555 requirements.



556

557 **Figure 15:** Scatter plots of OMI (left) and TROPOMI (right) versus MAX-DOAS data for the daily (top) and monthly
 558 (bottom) medians of collocated data. The correlation, slope and intercept of a linear regression using the robust Teil-Shein
 559 estimator is given as inset and plotted as a blue line. The black dotted line is the 1:1 line. The color indicates the latitude of the station. [$\text{Pmolec.cm}^{-2} = 10^{15} \text{ molec.cm}^{-2}$].
 560

561 **Table 3:** Summary of validation results for OMI and TROPOMI when considering all collocated pairs (daily or monthly
 562 means) together. Values for HCHO columns lower or larger than $8 \times 10^{15} \text{ molec.cm}^{-2}$ are given in brackets.

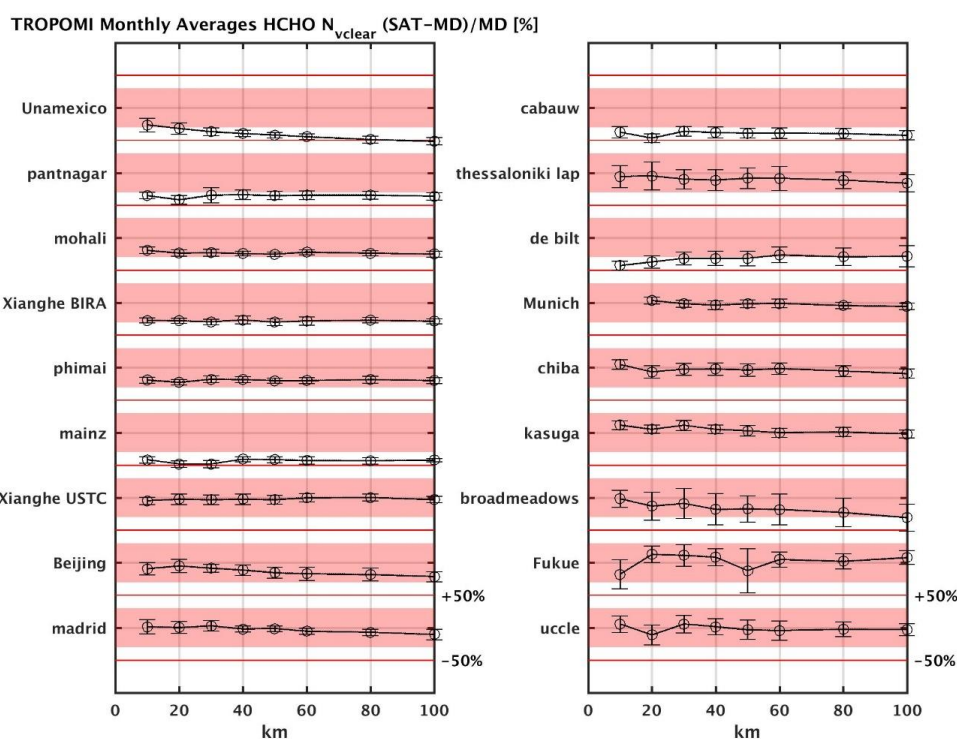
	OMI (<, > $8 \times 10^{15} \text{ molec.cm}^{-2}$)	TROPOMI (<, > $8 \times 10^{15} \text{ molec.cm}^{-2}$)
Daily		
MAD [$10^{15} \text{ molec.cm}^{-2}$]	7.3 (6.7, 7.9)	3.8 (3, 4)
Bias+ErrB [%]	-18±7.5 (-7+-12,-21±6.9)	-11±3.6 (-10+-4.6, -25±2.8)
Offset [$10^{15} \text{ molec.cm}^{-2}$]	3.1	1.9
Slope	0.51	0.6
Correlation	0.45	0.76
Monthly		
MAD [$10^{15} \text{ molec.cm}^{-2}$]	2.6 (2.5, 3.2)	2.3 (1.4, 2.7)
Bias+ErrB [%]	-9±13 (9±16.6, -24±12)	-12±8.6 (-5±10, -25±5.7)
Offset [$10^{15} \text{ molec.cm}^{-2}$]	2.9	1.7
Slope	0.57	0.64
Correlation	0.74	0.85

563 5.2 Sensitivity tests

564 We performed a few sensitivity tests, in order to evaluate the robustness of the validation results. First, we have used
 565 different radii around the stations (from 10 to 100km), in order to detect possible spatial resolution effects. Results are
 566 presented in Figure 16, for the TROPOMI case. At most stations, the bias shows marginally small dependency on the
 567 radius. Again, this points to the large natural dispersion of the HCHO columns. We find an important exception at the



568 UNAM station in Mexico, where the bias clearly increases with the radius (-30% at 10km, -50% at 100km). At this
569 location, the correlation and MADs are also improved at 10km (not shown). In Beijing and Broadmeadows, we do
570 observe an increase of the bias at 100km resolution, but the values at 10 and 20km are mostly equivalent. We
571 performed the same test with OMI, and found consistent results, except that the lower sampling does not allow using
572 a 10km-radius area.



573

574 **Figure 16: Median monthly bias as a function of the radius taken around the validation sites. Pink areas indicate 40%**
575 **bias.**

576 We also evaluated the impact of clouds using two further tests: (1) compare the daily TROPOMI validation results for
577 N_v and N_{v_clear} , (2) use a much stricter cloud filter on cloud radiance fractions (CRF) of 20% instead of 60%
578 (equivalent to an effective cloud fraction of 10% instead of 40%). With this strict cloud filter, there is no difference
579 between N_v and N_{v_clear} . Results are summarized in Table 4. These tests indicate that the TROPOMI HCHO
580 validation results do not change significantly when a cloud correction is applied, although the N_{v_clear} results are
581 slightly better. Using a more stringent cloud filter reduces the number of observations. The bias for the lowest columns
582 becomes positive (from -10 to +3%), and the offset is increased (from 1.9 to 2.6×10^{15} molec. cm^{-2}), while the negative
583 bias for the largest columns remains equivalent. These numbers will have to be re-evaluated using only the version 2
584 of the TROPOMI level 2 products available since July 2020, when enough data will be available. However, we note
585 that this limited impact of the cloud correction on the HCHO columns appears to be consistent with previous satellite



586 datasets, independently of the cloud product, as already observed with GOME-2 and OMI, using version 1 of the O2–
 587 O2 cloud product (De Smedt et al., 2015).

588 **Table 4: Summary of daily validation results for TROPOMI when considering all collocated pairs when using N_{v_clear}**
 589 **(first column), (1) when using N_v (second column) or (2) when using a strict cloud filter (third column).**

	TROPOMI N_{v_clear} ($<, >8 \times 10^{15}$ molec.cm $^{-2}$)	TROPOMI N_v ($<, >8 \times 10^{15}$ molec.cm $^{-2}$)	TROPOMI N_{v_clear} CRF<20% ($<, >8 \times 10^{15}$ molec.cm $^{-2}$)
Daily			
MAD [10^{15} molec.cm $^{-2}$]	3.8 (3, 4)	3.9 (3, 4.4)	3.3 (2.6, 3.9)
Bias±ErrB [%]	-11±3.6 (-10+/-4.6, -25±2.8)	-14±3.9 (-12±4.4,-29±2.9)	-3±4.6 (3±6.1, -27±3.8)
Offset [10^{15} molec.cm $^{-2}$]	1.9	1.8	2.6
Slope	0.6	0.56	0.57
Correlation	0.76	0.74	0.75

590 5.3 Effect of vertical smoothing

591 Three MAX-DOAS stations (Uccle, Xianghe BIRA-IASB, and UNAM) provide retrieved and a priori vertical profiles
 592 together with corresponding averaging kernels ([GEOMS format](#)). This allows taking into account the different vertical
 593 sensitivity of MAX-DOAS and TROPOMI measurements when making comparisons. We follow the methodology
 594 from Rodgers and Connor (2003) described in detail in Vigouroux et al. (2020). It consists of two steps: first taking
 595 into account the different a priori profiles used to retrieve these two data sets (Eq. 2 of Vigouroux et al., 2020), then
 596 smoothing the ground-based profiles using TROPOMI averaging kernels (Eq. 3 of Vigouroux et al., 2020).

597 We give in Table 5 the MAD and biases obtained before and after application of the methodology, for the daily mean
 598 comparisons. Note that the numbers at each site are slightly different than the ones obtained in sect. 5.1 (Figs. 5.3 and
 599 5.5) because the collocated pairs are constructed slightly differently: each collocated pixel of the satellite must be
 600 compared to MAX-DOAS before the daily average because the TROPOMI averaging kernel differs for each pixel.

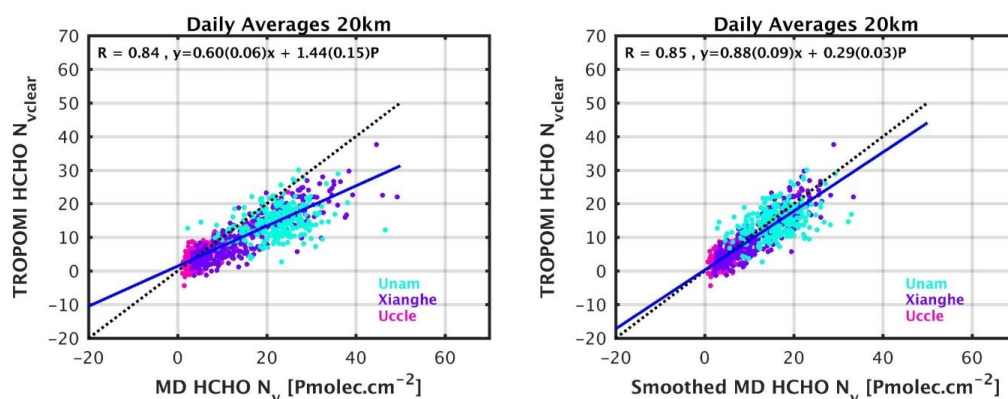
601 We see in Table 5 that at the cleanest site (Uccle) the effect of the smoothing is small, while at the more polluted sites
 602 Xianghe and UNAM, the biases are strongly reduced by about 20%. This result is in agreement with previous MAX-
 603 DOAS validation studies (De Smedt et al., 2015; Wang et al., 2019b), but also with aircraft and regional model
 604 comparisons (Zhu et al., 2020; Su et al., 2020). The effect of the smoothing is also clearly seen in Figure 17 where the
 605 scatter plots of daily comparisons between TROPOMI and MAX-DOAS are shown before and after vertical
 606 smoothing. The strong effect of the smoothing is usually not observed with FTIR comparisons because TROPOMI
 607 and FTIR measurements have similar vertical sensitivity, which rapidly drops in the atmospheric layers lower than
 608 3km (Vigouroux et al., 2020), while the MAX-DOAS shows an opposite sensitivity that is maximum at the surface
 609 and generally becomes negligible above 3km (Vigouroux et al., 2008; De Smedt et al., 2015; Wang et al., 2019a).
 610 This highlights the importance of taking into account the different a priori profiles and averaging kernels when
 611 comparing techniques having different vertical sensitivity.

612 **Table 5: Effect of a priori substitution and vertical smoothing on the daily comparisons of TROPOMI and MAX-DOAS**
 613 **data.**

Daily	Direct comparisons		Rodgers and Connor (2003) applied (a priori substitution and smoothing)	
	MAD [10^{15} molec.cm $^{-2}$]	BIAS ± Err_B [%]	MAD [10^{15} molec.cm $^{-2}$]	BIAS ± Err_B [%]



Uccle	2.4	-9.4 ± 5.8	2.4	-10.6 ± 5.5
Xianghe, BIRA	3.9	-32.2 ± 2.5	2.7	-9.1 ± 3.0
UNAM	6.1	-34.3 ± 3.2	5.8	-5.8 ± 5.7
	Scatter plot 3 sites		Scatter plot 3 sites	
Offset [10^{15} molec. cm^{-2}]	1.44		0.29	
Slope	0.60		0.88	
Correlation	0.84		0.85	

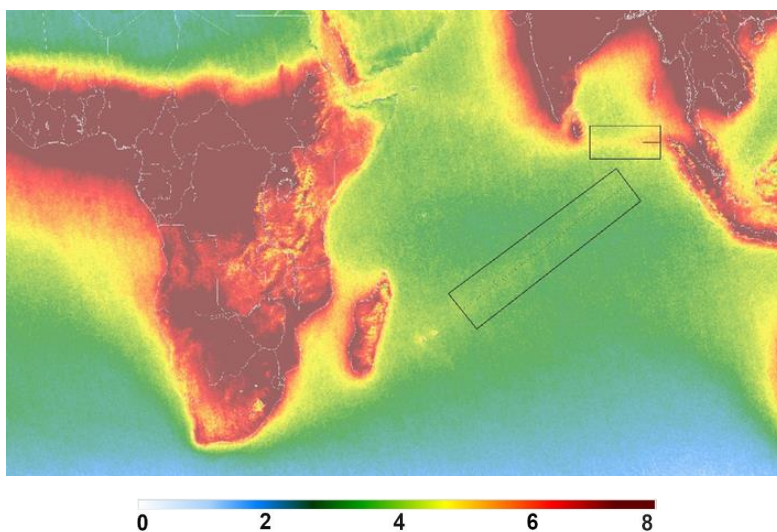


614

615 **Figure 17: Scatter plots of TROPOMI versus MAX-DOAS data for the daily means of collocated data before (left) and**
 616 **(right) vertical smoothing of the MAX-DOAS profile in Uccle, Xianghe and UNAM/Mexico. The correlation, slope and**
 617 **intercept of a linear regression using the robust Teil-Shein estimator is given inset and plotted as a blue line. The black**
 618 **dotted line is the 1:1 line. [$\text{Pmolec.cm}^{-2} = 10^{15}$ molec. cm^{-2}].**

619 **6 Detection of weak HCHO columns over shipping lanes**

620 As shown above, TROPOMI HCHO observations feature an unprecedented level of precision allowing for an
 621 improved detection of small columns at short time scales. Here, we present a case study to illustrate the ability of
 622 TROPOMI to detect small HCHO signals related to shipping emissions. When inspecting TROPOMI maps averaged
 623 over several months, weak lines of HCHO columns become visible over the background, especially in the Indian
 624 Ocean (see e.g. Figure 5). This becomes even clearer when saturating the continental HCHO columns by setting a
 625 lower maximum scale, as in Figure 18, which shows HCHO columns seasonally averaged over the months December,
 626 January and February between 2018 and 2021.



627

628

629 **Figure 18: Seasonal DJF map of TROPOMI HCHO tropospheric columns between Dec. 2018 and Feb.2021, on a spatial**
630 **grid of 0.05° in latitude and longitude. Observations are only filtered using the provided qa_values >0.5. (max.scale: 8x10¹⁵**
631 **molec.cm⁻²).**

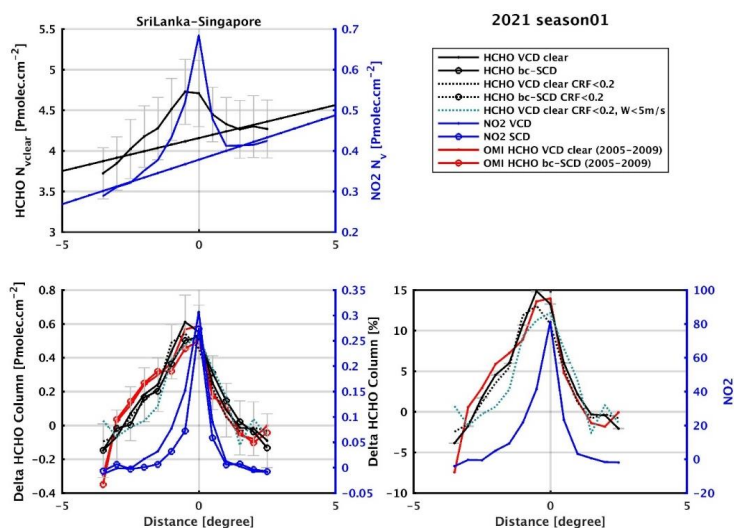
632 The detection of shipping emissions with satellite observations has often been reported for NO₂ (see for example
633 Beirle et al., 2004; Richter et al., 2004; 2011; Boersma et al., 2015; Georgoulas et al., 2020), and more recently also
634 for SO₂ based on OMI measurements (Theys et al., 2015). In the case of HCHO, however, only one study pointed to
635 the identification of a shipping lane signal detected in a 7-year average of ERS-2 GOME data in the ship track corridor
636 from Sri Lanka to Singapore (Marbach et al., 2009).

637 Here, we study two lines (1) from Sri Lanka to Singapore and (2) from Madagascar to Singapore. We perform an
638 analysis and several sensitivity tests in order to gain confidence and information on the enhanced HCHO. As illustrated
639 in the first panel of Figure 19 (line 1) and Figure 20 (line 2), in each box, we average the HCHO columns along the
640 ship track to obtain a spatial cross section, and we bin the data as a function of the distance from the line (distances
641 are expressed in degrees per 0.5° bin). The background level is not constant, for example due to continental outflow
642 in the Bay of Bengal, and needs to be removed. To do so, we fit a straight line through the column values at the edges
643 of the box and subtract this line from the signal. This allows to isolate a differential column and to evaluate its absolute
644 and relative magnitude compared to the background (respectively shown in the second and third panels of Figure 19
645 and Figure 20. For comparison, we perform the same analysis using TROPOMI NO₂ tropospheric columns from the
646 operational product (NO₂ ATBD, Van Geffen et al., 2020). Although only about half as wide, the localisation of the
647 NO₂ peak is found to be well aligned with the HCHO signal. Along the line from Sri Lanka to Singapore, we find a
648 similar column enhancement and plume width as in Marbach et al. (2009).

649 In order to exclude a possible indirect AMF effect caused by the TM5 a priori profiles, the same analysis is done based
650 on background-corrected slant columns (bc-SCD). We also restrict the analysis to clear sky observations, by using a
651 strict cloud filtering of CRF<20%. Furthermore, we use the wind vector information provided in the TROPOMI L2
652 product from version 2 onwards (from August 2020), to select only clear-sky observations with low wind conditions

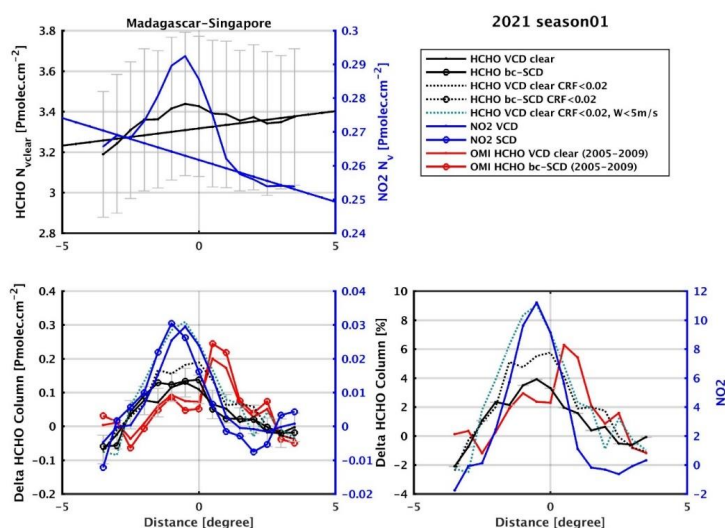


653 (qa>0.5, CRF<20%, W<5m/s). Finally, we add to the analysis a climatology of HCHO observations based on OMI
 654 measurements (2005-2009).



655

656 **Figure 19:** Box average for the first selected line between Sri Lanka and Singapore between Dec. 2020 and Feb. 2021. The
 657 x-axis represents the distance (south-north) in degrees from the shipping lane. The first panel shows the HCHO (in black)
 658 and NO₂ (in blue) tropospheric columns, binned per distance from the line center. The fitted lines are used to remove the
 659 background contribution. The two bottom panels present the absolute (left) and relative (right) column deviations from the
 660 background line. The analysis is performed on the slant and the vertical columns (circles/lines), using a stricter cloud
 661 filtering (CRF<20%, black dotted line), an additional filter on the wind velocity (W<5m/s, green dotted line), and finally on
 662 OMI observations averaged between 2005 and 2009 (red). [Pmolec.cm⁻² = 1x10¹⁵ molec.cm⁻²].

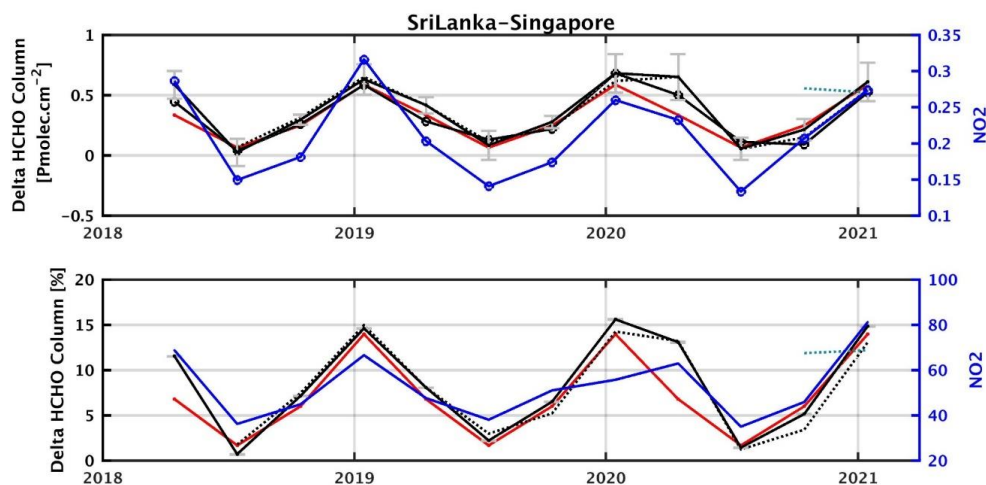


663

664 **Figure 20:** Same as Figure 19 for the second selected line between Madagascar and Singapore.

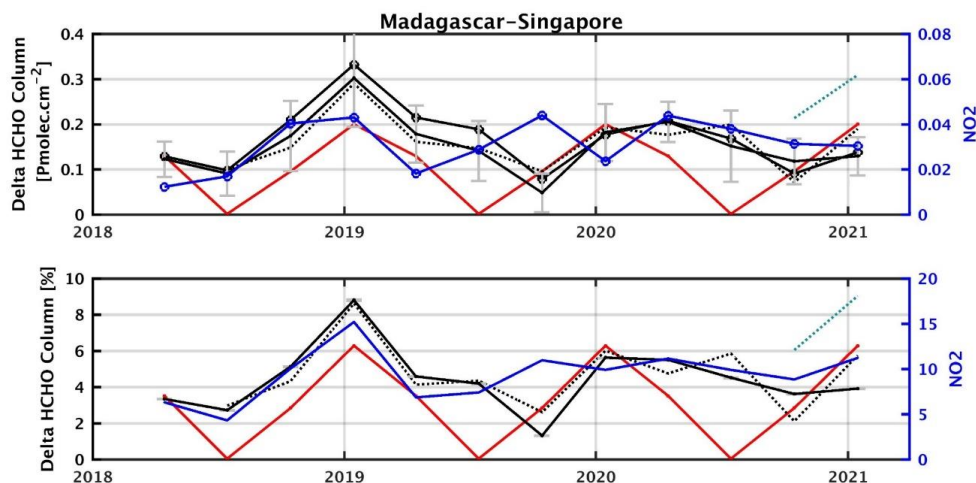


665 Using this approach, we analysed HCHO datasets for each season between MAM 2018 and DJF 2021. The absolute
666 and relative magnitude of the largest detected signal is plotted as a function of the season in Figure 21 and Figure 22.
667 Along the two lines, the signal is detected in the slant columns of HCHO and NO₂ as well. This excludes the possibility
668 of an artefact coming from the TM5 a priori profiles. The signal remains detectable in clear-sky observations, and is
669 even increased along the second line. We observe a similar effect of the wind speed filtering (last two seasons).
670 Selecting only low-wind conditions clearly enhances the signal along line 2, and during SON along line 1. The
671 magnitude of the detected HCHO signal is larger along line 1 (from 0.2 to 0.7x10¹⁵ molec.cm⁻², 15%) compared to
672 line 2 (from 0.1 to 0.3x10¹⁵ molec.cm⁻², 8%). We find that the absolute magnitude of the HCHO signal is larger than
673 the NO₂ signal by a factor 3 to 10, but the relative increase of the NO₂ columns is significantly larger: 60% along line
674 1 and 15% along line 2. Both lines show a clear seasonality, particularly in the HCHO columns, with a maximum
675 during the DJF seasons seen in the OMI climatology and in the TROPOMI 3-months averages. The HCHO signal
676 presents a clear drop in JJA along line 1. This is related to the wind direction and strength, which bring the line signal
677 closer to the HCHO continental outflow, making its detection more difficult. The OMI data need to be averaged over
678 several years in order to detect a significant signal. While the first line is well detected in the 5-years OMI climatology,
679 the second line presents a smaller magnitude, a larger variability, and cannot be detected in the most recent years of
680 OMI measurements.



681

682 **Figure 21:** Seasonal variation of the absolute (top panel) and relative (center panel) column deviations of the TROPOMI
683 HCHO (black), OMI 2005-2009 climatology HCHO (red) and TROPOMI NO₂ (blue) tropospheric columns along the Sri
684 Lanka – Singapore line. For each season, the maximum deviation compared to the background is provided. The results of
685 the analysis are given for the slant and the vertical columns (circles/lines), using a stricter cloud filtering (CRF < 20%, black
686 dotted line), an additional filter on the wind velocity (W < 5 m/s, green dotted line). [Pmolec.cm⁻² = 1x10¹⁵ molec.cm⁻²].



687

688 **Figure 22: Same as Figure 21 along the Madagascar – Singapore line.**

689 Using TROPOMI HCHO observations averaged over 3 months, it is therefore possible to detect a signal as small as
690 0.1×10^{15} molec. cm^{-2} (with a median deviation of 0.03×10^{15} molec. cm^{-2}), after removal of the background contribution.
691 Note that along the first line a similar analysis can also be performed on a monthly basis. While we show several
692 evidences that the signal is related to shipping emissions, its source is not studied here. As discussed in Marbach et al.
693 (2009) it could be due to secondary HCHO production via the atmospheric oxidation of NMVOCs emitted from ship
694 engines but also to enhanced CH_4 oxidation by elevated levels of OH radicals within the ship plumes. Model analysis
695 suggest that the second hypothesis is the main factor responsible for the elevated HCHO levels (Song et al.; 2010).
696 Other HCHO lines can be detected as well in the Tropics, although weaker in magnitude or closer to the continental
697 outflow (in the South-West of Africa or in the West of India). More advanced techniques to separate the signal from
698 the background and to account for wind dispersion effects could help in detecting more shipping lanes but also weak
699 continental emissions (Beirle et al., 2004).

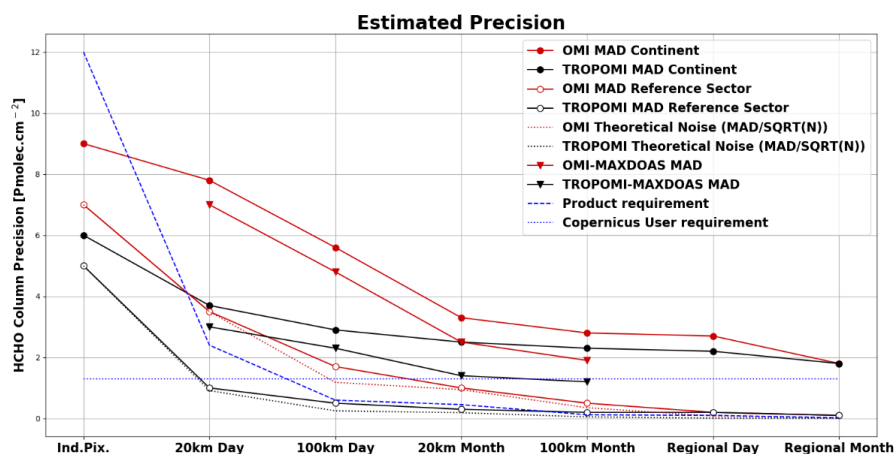
700 7 Conclusions

701 Owing to its high spatial resolution resulting in many measurement points, coupled with an improved signal to noise
702 ratio at single pixel level, TROPOMI allows to monitor HCHO tropospheric columns from space with an
703 unprecedented definition. The global and regional maps show a clear reduction of the noise compared to previous
704 sensors, allowing for the detection of weaker HCHO signals, and the monitoring of HCHO variations on a much
705 shorter time scale.

706 We have evaluated the TROPOMI HCHO operational product against the QA4ECV OMI HCHO dataset, and against
707 a network of 18 ground-based MAX-DOAS instruments. The gain in precision at different spatial and temporal scales
708 was estimated by (1) comparing the median deviation of the averaged columns, and (2) validating the data using
709 MAX-DOAS column network measurements. Both methods include additional noise components from temporal



710 variation, spatial variation and ground-based column precision. Results are summarized in Figure 23 where precision
711 estimates are provided for observations over regions with enhanced continental emission and for background
712 conditions, as a function of the time resolution (daily or monthly averages) and of the spatial resolution (from 20km
713 to regional scale). At 20 and 100km resolution, both the median deviation approach and the validation results lead to
714 very consistent estimates of the precision. The theoretical noise is also represented in the figure; it decreases as the
715 squared root of the number of observations included in the averages. In remote conditions, the median deviation of
716 the averaged columns follows closely the theoretical noise until reaching a threshold. If we consider a large region in
717 the reference sector, all estimates converge towards a limit of about 0.2×10^{15} molec.cm⁻² molec.cm⁻² (day) to 0.1×10^{15}
718 molec.cm⁻² (month) both for OMI and TROPOMI. Over continental emission sources, the reduction of the noise is
719 counterbalanced by the HCHO natural variability and by other source of pseudo-noise which depend on the spatial
720 and temporal scales of the observations. The largest improvement brought by TROPOMI is found for daily
721 observations at 20km resolution, for which a gain in precision by a factor of 3 is obtained compared to OMI. The
722 product and COPERNICUS user requirements for precision are also represented in the figure. Both are reached with
723 TROPOMI using daily averaged data at the resolution of 20km if we consider the dispersion in remote regions.
724 However, over continental emissions, local variability effects added up to the estimated precision that reaches a
725 threshold of about 2×10^{15} molec.cm⁻².



726

727 **Figure 23: Estimated precision of OMI (in red) and TROPOMI (in black) HCHO columns at different spatial and temporal**
728 **scales (20km, 100km, regions, day/month). The median deviation of the satellite HCHO columns are provided for**
729 **continental emissions (plain circles) and in the remote reference sector (white circles). Validation estimates are plotted at**
730 **20km and 100km (MAD of differences between satellite and MAX-DOAS columns, triangles). The theoretical noise (dotted**
731 **lines) corresponds to single measurement precision divided by the square root of observations. The dashed blue line is the**
732 **TROPOMI product requirement, based on a single measurement precision of 12×10^{15} molec.cm⁻². The horizontal blue line**
733 **at 1.3×10^{15} molec.cm⁻² represents the COPERNICUS user requirement. [Pmolec.cm⁻² = 1×10^{15} molec.cm⁻²].**

734 For the HCHO absolute values, we show that OMI and TROPOMI observations agree very well for moderate to large
735 HCHO levels (columns larger than 5×10^{15} molec.cm⁻²) for which the bias between both datasets is smaller than 10%.
736 For lower columns however, OMI observations present a remaining bias of about +20% compared to TROPOMI. This
737 good agreement is obtained by considering vertical columns calculated with air mass factors not corrected for cloud



738 effects (clear VCD). This allows to avoid biases related to differences in the cloud products. For all applications that
739 require combining the OMI and TROPOMI observations for low to moderate cloud fractions, we therefore advise to
740 use clear VCDs. Validation results confirm the good agreement between the OMI and TROPOMI datasets and a
741 similar underestimation of both products in the highest range of the HCHO levels (-25% in average for columns larger
742 than 8×10^{15} molec.cm⁻²). For medium columns, OMI presents a slight overestimation compared to MAX-DOAS data,
743 which is not observed for TROPOMI. Sensitivity tests show that validation results obtained with the TROPOMI
744 HCHO columns are weakly dependent on the cloud correction. They also depend weakly on the radius considered
745 around the station, with a few exceptions such as Mexico city or coastal stations. On the contrary, the vertical
746 smoothing (tested at three stations) has a strong effect on the comparison with MAX-DOAS. After taking into account
747 the different a priori profiles and averaging kernels, the bias for large HCHO columns is strongly reduced by about
748 20%.

749 Comparing OMI and TROPOMI monthly averaged HCHO columns, we do not observe significant differences related
750 to the spatial resolution, except in regions surrounded by natural boundaries where the benefit of the finer spatial
751 resolution of TROPOMI is clearly apparent. The weak sensitivity to the spatial resolution of HCHO measurements
752 can be understood when considering that HCHO is a secondary product from the degradation of NMOVCs with
753 various lifetimes, which results in a general spread of the HCHO spatial distributions. The large number of TROPOMI
754 observations allows to perform validation at a resolution as small as 10km on a daily basis with a sufficient precision,
755 which is not possible with OMI. It is clear that TROPOMI brings a significant improvement in the temporal resolution
756 of the observations. At most of the validation sites, TROPOMI allows for daily validation results as robust as those
757 obtained with OMI on a monthly basis.

758 The number of ground-based stations providing MAX-DOAS HCHO observations is constantly growing, providing
759 a large range of observation conditions, and for some of them, over several years allowing the comparisons of the
760 performances of several satellite datasets. Note however that the lower range of HCHO levels is under-represented,
761 as well as some of the largest emission regions such as South America or Africa. Following the validation study of
762 Vigouroux et al. (2020) based on a FTIR network of instruments, this study illustrates again the added value of using
763 a large network of instruments to draw more robust conclusions. FTIR and MAX-DOAS networks are complementary
764 to each other and could be combined to cover as many conditions as possible. Similarly to what was achieved for the
765 FTIR network, the MAX-DOAS HCHO datasets would benefit from further homogenisation efforts.

766 Finally, to illustrate the benefit of TROPOMI for the detection of small HCHO signals, we present a case study
767 addressing the detection of shipping lanes in the Indian Ocean. Using simultaneous observations of tropospheric NO₂
768 and meteorological wind field data, we present strong evidences for an HCHO production in regions affected by
769 shipping emissions. Owing to the sensitivity of TROPOMI, such small signals can now be observed from space on a
770 seasonal basis.

771 **Code and data availability**



772 The S5p HCHO data are available at <https://scihub.copernicus.eu>. The access and use of any Copernicus Sentinel data available
773 through the Copernicus Sentinel Data Hub is governed by the Legal Notice on the use of Copernicus Sentinel Data and Service
774 Information and is given here: https://sentinels.copernicus.eu/documents/247904/690755/Sentinel_Data_Legal_Notice.
775 The QA4ECV OMI HCHO product is available at <https://doi.org/10.18758/71021031> (De Smedt et al., 2017). The MAX-DOAS
776 datasets can be requested from the individual PIs of each station.

777 Author contributions

778 IDS coordinated the paper and carried out the analysis. GP and CV are PIs of the NIDFORVAL S5PVT project, SC ensures the
779 MPC routine validation. IDS, PH, YH, CLe, DL, FR, NT, JV, MVR developed the TROPOMI HCHO product. FB, IDS, YH, AR,
780 MVR, TW developed the QA4ECV OMI HCHO product. AB, NB, KLC, SD, FH, HI, VK, CLi, AP, CRC, RGR, MVR, TW are
781 PIs for the QA4ECV MAX-DOAS measurements. BL, SC, GP, CV performed MAX-DOAS data collection and format
782 harmonization and carried out the validation analysis. SC, KUE and JCL are responsible of the MPC routine validation. MVR is
783 the coordinator of this research. All co-authors revised and commented on the paper.

784 Acknowledgements

785 This work contains modified Copernicus Sentinel-5 Precursor satellite data (2018-2020) post-processed by BIRA-IASB. Part of
786 the reported work was carried out in the framework of the Copernicus Sentinel-5 Precursor Mission Performance Centre (S5p
787 MPC), contracted by the European Space Agency (ESA/ESRIN, Contract No. 4000117151/16/I-LG) and supported by the Belgian
788 Federal Science Policy Office (BELSPO), the Royal Belgian Institute for Space Aeronomy (BIRA-IASB) and the German
789 Aerospace Centre (DLR). BIRA-IASB acknowledges national funding from BELSPO and ESA through the ProDEX projects
790 TRACE-S5P (TRACE-S5P project) and TROVA. Part of this work was carried out also in the framework of the S5p Validation
791 Team (S5PVT) AO projects NIDFORVAL (ID #28607, PI G. Pinaridi, C. Vigouroux, BIRA-IASB). Multi-sensor HCHO
792 developments have been funded by the EU FP7 QA4ECV project (grant no. 607405), in close cooperation with KNMI, University
793 of Bremen, MPIC-Mainz and WUR. Work by H. Irie was supported by the Environment Research and Technology Development
794 Fund (JPMEERF20192001 and JPMEERF20215005) of the Environmental Restoration and Conservation Agency of Japan, JSPS
795 KAKENHI (grant numbers JP19H04235 and JP20H04320), and the JAXA 2nd research announcement on the Earth Observations
796 (grant number 19RT000351). We acknowledge Mark Wenig from LMU for supporting the MAX-DOAS operations in Munich,
797 Caroline Fayt and Christian Herman from BIRA-IASB for the Uccle and Xianghe instruments, as well as Pucái Wang from
798 IAP/CAS for maintaining the BIRA-IASB instrument in Xianghe. We thank Alejandro Bezanilla from CCA-UNAM, Manish Naia
799 from ARIES for the MAX-DOAS instrument operation in Pantnager and Thanawat Jarupongsakul from Chulalongkorn University
800 for the Phimai station. We acknowledge IISER Mohali Atmospheric Chemistry Facility for supporting the MAX-DOAS operations
801 in Mohali.

802 References

803 Alvarado, L. M. A., Richter, A., Vrekoussis, M., Hilboll, A., Kalisz Hedegaard, A. B., Schneising, O., and Burrows,
804 J. P.: Unexpected long-range transport of glyoxal and formaldehyde observed from the Copernicus Sentinel-5



- 805 Precursor satellite during the 2018 Canadian wildfires, *Atmos. Chem. Phys.*, 20, 2057–2072,
806 <https://doi.org/10.5194/acp-20-2057-2020>, 2020.
- 807 Arellano, J., Krüger, A., Rivera, C., Stremme, W., Friedrich, M., Bezanilla, A., and Grutter, M.: The MAX-DOAS
808 network in Mexico City to measure atmospheric pollutants, *Atmosfera*, 29,157–167,
809 <https://doi.org/10.20937/ATM.2016.29.02.05>, 2016.
- 810 Barkley, M. P., González Abad, G., Kurosu, P. T., Spurr, R., Torbatian, S. and Lerot, C.: OMI air-quality monitoring
811 over the Middle East, *Atmos. Chem. Phys.*, 17(7), 4687–4709, doi:10.5194/acp-17-4687-2017, 2017.
- 812 Bauwens, M., Stavrou, T., Müller, J.-F., De Smedt, I., Van Roozendael, M., van der Werf, G. R., Wiedinmyer, C.,
813 Kaiser, J. W., Sindelarova, K., and Guenther, A.: Nine years of global hydrocarbon emissions based on source
814 inversion of OMI formaldehyde observations, *Atmos. Chem. Phys.*, 16, 10133–10158, [https://doi.org/10.5194/acp-](https://doi.org/10.5194/acp-16-10133-2016)
815 [16-10133-2016](https://doi.org/10.5194/acp-16-10133-2016), 2016.
- 816 Beirle, S., Platt, U., von Glasow, R., Wenig, M., and Wagner, T. : Estimate of nitrogen oxide emissions from shipping
817 by satellite remote sensing, *Geophys. Res. Lett.*, 31, L18102, doi:10.1029/2004GL020312, 2004.
- 818 Beirle, S., Borger, C., Dörner, S., Li, A., Hu, Z., Liu, F., Wang, Y. and Wagner, T.: Pinpointing nitrogen oxide
819 emissions from space, *Sci. Adv.*, 5(11), eaax9800, doi:10.1126/sciadv.aax9800, 2019.
- 820 Benavent, N., Garcia-Nieto, D., Wang, S. and Saiz-Lopez, A.: MAX-DOAS measurements and vertical profiles of
821 glyoxal and formaldehyde in Madrid, Spain, *Atmos. Environ.*, 199, 357–367,
822 doi:<https://doi.org/10.1016/j.atmosenv.2018.11.047>, 2019.
- 823 Boersma, K. F., Eskes, H. J., and Brinksma, E. J.: Error analysis for tropospheric NO₂ retrieval from space, *J.*
824 *Geophys. Res.*, 109, <https://doi.org/10.1029/2003JD003962>, 2004.
- 825 Boersma, K. F., Vinken, G. C. M. and Tournadre, J.: Ships going slow in reducing their NO_x emissions: changes in
826 2005–2012 ship exhaust inferred from satellite measurements over Europe, *Environ. Res. Lett.*, 10(7), 074007,
827 doi:10.1088/1748-9326/10/7/074007, 2015.
- 828 Boersma, K. F., Eskes, H. J., Richter, A., Smedt, I. De, Lorente, A., Beirle, S., Van Geffen, J. H. G. M., Zara, M.,
829 Peters, E., Roozendael, M. Van and others: Improving algorithms and uncertainty estimates for satellite NO₂
830 retrievals: results from the quality assurance for the essential climate variables (QA4ECV) project, *Atmos. Meas.*
831 *Tech.*, 11(12), 6651–6678, 2018.
- 832 Bösch, T., Rozanov, V., Richter, A., Peters, E., Rozanov, A., Wittrock, F., Merlaud, A., Lampel, J., Schmitt, S., de
833 Haij, M., 20Berkhout, S., Henzing, B., Apituley, A., den Hoed, M., Vonk, J., Tiefengraber, M., Müller, M.,
834 and Burrows, J. P.: BOREAS –a new MAX-DOAS profile retrieval algorithm for aerosols and trace gases, *Atmos.*
835 *Meas. Tech.*, 11, 6833–6859, <https://doi.org/10.5194/amt-11-6833-2018>, 2018.
- 836 Bovensmann, H., Peuch, V.-H., van Weele, M., Erbetseder, T., and Veihelmann, B.: Report Of The Review Of User
837 Requirements For Sentinels-4/-5, ESA, EOP-SM/2281/BV-bv, issue: 1.2, 2011.



- 838 Brinksma, E. J., Pinardi, G., Volten, H., Braak, R., Richter, A., Scho, A., Van Roozendael, M., Fayt, C., Hermans, C.,
839 Dirksen, R. J., Vlemmix, T., Berkhout, A. J. C., Swart, D. P. J., Oetjen, H., Wittrock, F., Wagner, T., Ibrahim, O. W.,
840 Leeuw, G. De, Moerman, M., Curier, R. L., Celarier, E. A., Cede, A., Knap, W. H., Veefkind, J. P., Eskes, H. J.,
841 Allaart, M., Rothe, R., Piters, A. and Levelt, P. F.: The 2005 and 2006 DANDELIONS NO₂ and aerosol
842 intercomparison campaigns, *J. Geophys. Res.*, 113(D16), 1–18, doi:10.1029/2007JD008808, 2008.
- 843 Cao, H., Fu, T.-M., Zhang, L., Henze, D. K., Miller, C. C., Lerot, C., Abad, G. G., Smedt, I. De, Zhang, Q.,
844 Roozendael, M. van and others: Adjoint inversion of Chinese non-methane volatile organic compound emissions using
845 space-based observations of formaldehyde and glyoxal, *Atmos. Chem. Phys.*, 18(20), 15017–15046, 2018.
- 846 Chan, K. L., Wang, Z., Ding, A., Heue, K.-P., Shen, Y., Wang, J., Zhang, F., Shi, Y., Hao, N., and Wenig, M.: MAX-
847 DOAS measurements of tropospheric NO₂ and HCHO in Nanjing and a comparison to ozone monitoring instrument
848 observations, *Atmos. Chem. Phys.*, 19, 10051–10071, <https://doi.org/10.5194/acp-19-10051-2019>, 2019.
- 849 Chan, K. L., Wiegner, M., van Geffen, J., De Smedt, I., Alberti, C., Cheng, Z., Ye, S., and Wenig, M.: MAX-DOAS
850 measurements of tropospheric NO₂ and HCHO in Munich and the comparison to OMI and TROPOMI satellite
851 observations, *Atmos. Meas. Tech.*, 13, 4499–4520, <https://doi.org/10.5194/amt-13-4499-2020>, 2020.
- 852 Chance, K. V., Palmer, P. I., Martin, R. V., Spurr, R. J. D., Kurosu, T. P. and Jacob, D. J.: Satellite observations of
853 formaldehyde over North America from GOME, *Geophysical Research Letters*, 27(21), 3461–3464,
854 doi:10.1029/2000GL011857, 2000.
- 855 Chan Miller, C., Jacob, D. J., Marais, E. A., Yu, K., Travis, K. R., Kim, P. S., Fisher, J. A., Zhu, L., Wolfe, G. M.,
856 Hanisco, T. F., Keutsch, F. N., Kaiser, J., Min, K.-E., Brown, S. S., Washenfelder, R. A., González Abad, G., and
857 Chance, K.: Glyoxal yield from isoprene oxidation and relation to formaldehyde: chemical mechanism, constraints
858 from SENEX aircraft observations, and interpretation of OMI satellite data, *Atmos. Chem. Phys.*, 17, 8725–8738,
859 <https://doi.org/10.5194/acp-17-8725-2017>, 2017.
- 860 Choi, Y. and Souri, A. H.: Seasonal behavior and long-term trends of tropospheric ozone, its precursors and chemical
861 conditions over Iran: A view from space, *Atmos. Environ.*, 106, 232–240,
862 doi:<https://doi.org/10.1016/j.atmosenv.2015.02.012>, 2015.
- 863 Clémer, K., Van Roozendael, M., Fayt, C., Hendrick, F., Hermans, C., Pinardi, G., Spurr, R., Wang, P. and De
864 Mazière, M.: Multiple wavelength retrieval of tropospheric aerosol optical properties from MAX-DOAS
865 measurements in Beijing, *Atmos. Meas. Tech.*, 3, 863–878 [online] Available from: doi:10.5194/amt-3-863-2010,
866 2010.
- 867 Compernelle, S., Argyrouli, A., Lutz, R., Sneep, M., Lambert, J.-C., Fjæraa, A. M., Hubert, D., Keppens, A., Loyola,
868 D., O'Connor, E., Romahn, F., Stammes, P., Verhoelst, T. and Wang, P.: Validation of the Sentinel-5 Precursor
869 TROPOMI cloud data with Cloudnet, Aura OMI O₂-O₂, MODIS and Suomi-NPP VIIRS, *Atmos. Meas. Tech.*
870 *Discuss.*, (June), 1–33, doi:10.5194/amt-2020-122, 2020.



- 871 De Smedt, I., Müller, J.-F., Stavrakou, T., van der A, R., Eskes, H. and Van Roozendael, M.: Twelve years of global
872 observations of formaldehyde in the troposphere using GOME and SCIAMACHY sensors, *Atmos. Chem. Phys.*,
873 8(16), 4947-4963, 2008.
- 874 De Smedt, I., Stavrakou, T., Müller, J. F., van Der A, R. J. and Van Roozendael, M.: Trend detection in satellite
875 observations of formaldehyde tropospheric columns, *Geophys. Res. Lett.*, 37(18), L18808,
876 doi:10.1029/2010GL044245, 2010.
- 877 De Smedt, I., Van Roozendael, M., Stavrakou, T., Müller, J.-F., Lerot, C., Theys, N., Valks, P., Hao, N., and
878 van der A, R.: Improved retrieval of global tropospheric formaldehyde columns from GOME-2/MetOp-A addressing
879 noise reduction and instrumental degradation issues, *Atmos. Meas. Tech. Discuss.*, 5, 5571-5616, doi:10.5194/amt-d-
880 5-5571-2012, Special Issue: GOME-2: calibration, algorithms, data products and validation, 2012.
- 881 De Smedt, I., Stavrakou, T., Hendrick, F., Danckaert, T., Vlemmix, T., Pinardi, G., Theys, N., Lerot, C., Gielen, C.,
882 Vigouroux, C., Hermans, C., Fayt, C., Veeffkind, P., Müller, J.-F., and Van Roozendael, M.: Diurnal, seasonal and
883 long-term variations of global formaldehyde columns inferred from combined OMI and GOME-2 observations,
884 *Atmos. Chem. Phys.*, 15, 12519-12545, doi:10.5194/acp-15-12519-2015, 2015
- 885 De Smedt, I., Yu, H., Richter, A., Beirle, S., Eskes, H., Boersma, K.F., Van Roozendael, M., Van Geffen, J., Lorente,
886 A. and Peters, E.: QA4ECV HCHO tropospheric column data from OMI (Version 1.1) [Data set], 2017.
- 887 De Smedt, I., Theys, N., Yu, H., Danckaert, T., Lerot, C., Compennolle, S., Van Roozendael, M., Richter, A., Hilboll,
888 A., Peters, E., Pedernana, M., Loyola, D., Beirle, S., Wagner, T., Eskes, H., van Geffen, J., Boersma, K. F., and
889 Veeffkind, P.: Algorithm theoretical baseline for formaldehyde retrievals from S5P TROPOMI and from the QA4ECV
890 project, *Atmos. Meas. Tech.*, 11, 2395–2426, <https://doi.org/10.5194/amt-11-2395-2018>, 2018.
- 891 Dimitropoulou, E., Hendrick, F., Pinardi, G., Friedrich, M. M., Merlaud, A., Tack, F., De Longueville, H., Fayt, C.,
892 Hermans, C., Laffineur, Q., Fierens, F., and Van Roozendael, M.: Validation of TROPOMI tropospheric NO₂ columns
893 using dual-scan multi-axis differential optical absorption spectroscopy (MAX-DOAS) measurements in Uccle,
894 Brussels, *Atmos. Meas. Tech.*, 13, 5165–5191, <https://doi.org/10.5194/amt-13-5165-2020>, 2020.
- 895 Drosoglou, T., Bais, A. F., Zyrichidou, I., Kouremeti, N., Poupkou, A., Liora, N., Giannaros, C., Koukouli, M. E.,
896 Balis, D., and Melas, D.: Comparisons of ground-based tropospheric NO₂ MAX-DOAS measurements to satellite
897 observations with the aid of an air quality model over the Thessaloniki area, Greece, *Atmos. Chem. Phys.*, 17, 5829-
898 5849, <https://doi.org/10.5194/acp-17-5829-2017>, 2017.
- 899 ESA: Sentinel-5 Precursor Calibration and Validation Plan for the Operational Phase, ref: ESA-EOPG-CSCOP-PL-
900 0073, issue:1.1, 06/11/2017 (<https://sentinel.esa.int/documents/247904/2474724/Sentinel-5P-Calibration-and-Validation-Plan.pdf>).
- 902 Fortems-Cheiney, A., Chevallier, F., Pison, I., Bousquet, P., Saunois, M., Szopa, S., Cressot, C., Kurosu, T. P., Chance,
903 K. and Fried, A.: The formaldehyde budget as seen by a global-scale multi-constraint and multi-species inversion
904 system, *Atmos. Chem. Phys. Discuss.*, 12(3), 6909-6955, doi:10.5194/acpd-12-6909-2012, 2012.



- 905 Franco, B., Hendrick, F., Van Roozendael, M., Müller, J.-F., Stavrou, T., Marais, E. A., Bovy, B., Bader, W., Fayt,
906 C., Hermans, C., Lejeune, B., Pinardi, G., Servais, C., and Mahieu, E.: Retrievals of formaldehyde from ground-based
907 FTIR and MAX-DOAS observations at the Jungfraujoch station and comparisons with GEOS-Chem and IMAGES
908 model simulations, *Atmos. Meas. Tech.*, 8, 1733-1756, doi:10.5194/amt-8-1733-2015, 2015.
- 909 Franco, B., Blumenstock, T., Cho, C., Clarisse, L., Clerbaux, C., Coheur, P.-F., De Mazière, M., De Smedt, I., Dorn,
910 H.-P., Emmerichs, T., Fuchs, H., Gkatzelis, G., Griffith, D., et al.: Ubiquitous atmospheric production of organic acids
911 mediated by warm clouds, *Nature*, 2017-10-14339, 2021.
- 912 Friedrich, M. M., Rivera, C., Stremme, W., Ojeda, Z., Arellano, J., Bezanilla, A., García-Reynoso, J. A., and Grutter,
913 M.: NO₂ vertical profiles and column densities from MAX-DOAS measurements in Mexico City, *Atmos. Meas.*
914 *Tech.*, 12, 2545–2565, <https://doi.org/10.5194/amt-12-2545-2019>, 2019.
- 915 Frieß, U., Monks, P. S., Remedios, J. J., Rozanov, A., Sinreich, R., Wagner, T. and Platt, U.: MAX-DOAS O₄
916 measurements: A new technique to derive information on atmospheric aerosols: 2. Modeling studies, *J. Geophys. Res.*,
917 111(D14), doi:10.1029/2005JD006618, 2006.
- 918 Frieß, U., Klein Baltink, H., Beirle, S., Clèmer, K., Hendrick, F., Henzing, B., Irie, H., Leeuw, G. de, Li, A., Moerman,
919 M. M., Roozendael, M. van, Shaiganfar, R., Wagner, T., Wang, Y., Xie, P., Yilmaz, S. and Zieger, P.: Intercomparison
920 of aerosol extinction profiles retrieved from MAX-DOAS measurements, *Atmos. Meas. Tech.*, 9, 3205–3222,
921 <https://doi.org/10.5194/amt-9-3205-2016>, 2016.
- 922 Frieß, U., Beirle, S., Alvarado Bonilla, L., Bösch, T., Friedrich, M. M., Hendrick, F., Pitters, A., Richter, A., van
923 Roozendael, M., Rozanov, V. V., Spinei, E., Tirpitz, J.-L., Vlemmix, T., Wagner, T., and Wang, Y.: Intercomparison
924 of MAX-DOAS vertical profile retrieval algorithms: studies using synthetic data, *Atmos. Meas. Tech.*, 12, 2155-2181,
925 <https://doi.org/10.5194/amt-12-2155-2019>, 2019.
- 926 Georgoulias, A. K., Boersma, K. F., van Vliet, J., Zhang, X., van der A, R., Zanis, P. and de Laat, J.: Detection of NO₂
927 pollution plumes from individual ships with the TROPOMI/S5P satellite sensor, *Environ. Res. Lett.*, 15(12), 124037,
928 doi:10.1088/1748-9326/abc445, 2020.
- 929 Gielen, C., Hendrick, F., Pinardi, G., De Smedt, I., Fayt, C., Hermans, C., Stavrou, T., Bauwens, M., Müller, J.,
930 Ndenzako, E., Nzohabonayo, P., Akimana, R., Niyonzima, S., Van Roozendael, M. and De Mazière, M.:
931 Characterisation of Central-African aerosol and trace-gas emissions based on MAX-DOAS measurements and model
932 simulations over, *Atmos. Chem. Phys. Discuss.*, (2), 1–41, doi:10.5194/acp-2016-1104, 2017.
- 933 González Abad, G., Liu, X., Chance, K., Wang, H., Kurosu, T. P. and Suleiman, R.: Updated Smithsonian
934 Astrophysical Observatory Ozone Monitoring Instrument (SAO OMI) formaldehyde retrieval, *Atmos. Meas. Tech.*,
935 8(1), 19–32, doi:10.5194/amt-8-19-2015, 2015.
- 936 González Abad, G., Vasilkov, A., Seftor, C., Liu, X., and Chance, K.: Smithsonian Astrophysical Observatory Ozone
937 Mapping and Profiler Suite (SAO OMPS) formaldehyde retrieval, *Atmos. Meas. Tech.*, 9, 2797–2812,
938 <https://doi.org/10.5194/amt-9-2797-2016>, 2016.



- 939 Gonzalez Abad, G., Souri, A. H., Bak, J., Chance, K., Flynn, L. E., Krotkov, N. A., Lamsal, L., Li, C., Liu, X., Miller,
940 C. C., Nowlan, C. R., Suleiman, R. and Wang, H.: Five decades observing Earth's atmospheric trace gases using
941 ultraviolet and visible backscatter solar radiation from space, *J. Quant. Spectrosc. Radiat. Transf.*, 238, 106478,
942 doi:<https://doi.org/10.1016/j.jqsrt.2019.04.030>, 2019.
- 943 Hassinen, S., Balis, D., Bauer, H., Begoin, M., Delcloo, A., Eleftheratos, K., Gimeno Garcia, S., Granville, J., Grossi,
944 M., Hao, N., Hedelt, P., Hendrick, F., Hess, M., Heue, K.-P., Hovila, J., Jönch-Sørensen, H., Kalakoski, N., Kauppi,
945 A., Kiemle, S., Kins, L., Koukouli, M. E., Kujanpää, J., Lambert, J.-C., Lang, R., Lerot, C., Loyola, D., Pedergnana,
946 M., Pinardi, G., Romahn, F., Van Roozendaal, M., Lutz, R., De Smedt, I., Stammes, P., Steinbrecht, W., Tamminen,
947 J., Theys, N., Tilstra, L. G., Tuinder, O. N. E., Valks, P., Zerefos, C., Zimmer, W. and Zyrichidou, I.: Overview of the
948 O3M SAF GOME-2 operational atmospheric composition and UV radiation data products and data availability,
949 *Atmos. Meas. Tech.*, 9(2), 383–407, doi:10.5194/amt-9-383-2016, 2016.
- 950 Heckel, A., Richter, A., Tarsu, T., Wittrock, F., Hak, C., Pundt, I., Junkermann, W., and Burrows, J. P.: MAX-DOAS
951 measurements of formaldehyde in the Po-Valley, *Atmos. Chem. Phys.*, 5, 909–918, [http://www.atmos-chem-](http://www.atmos-chem-phys.net/5/909/2005)
952 [phys.net/5/909/2005](http://www.atmos-chem-phys.net/5/909/2005), 2005.
- 953 Hewson, W., Bösch, H., Barkley, M. P. and De Smedt, I.: Characterisation of GOME-2 formaldehyde retrieval
954 sensitivity, *Atmospheric Measurement Techniques*, 6(2), 371–386, doi:10.5194/amt-6-371-2013, 2013.
- 955 Hendrick, F., Müller, J.-F., Clémer, K., Wang, P., De Mazière, M., Fayt, C., Gielen, C., Hermans, C., Ma, J. Z.,
956 Pinardi, G., Stavrakou, T., Vlemmix, T. and Van Roozendaal, M.: Four years of ground-based MAX-DOAS
957 observations of HONO and NO₂ in the Beijing area, *Atmos. Chem. Phys.*, 14(2), 765–781, doi:10.5194/acp-14-765-
958 2014, 2014.
- 959 Honninger, G., von Friedeburg, C. and Platt, U.: Multi axis differential optical absorption spectroscopy (MAX-
960 DOAS), *Atmos. Chem. Phys.*, 4, 231–254, www.atmos-chem-phys.org/acp/4/231/, 2004.
- 961 Hoque, H. M. S., Irie, H., & Damiani, A. : First MAX-DOAS observations of formaldehyde and glyoxal in Phimai,
962 Thailand, *Journal of Geophysical Research: Atmospheres*, 123, 9957–9975, <https://doi.org/10.1029/2018JD028480>,
963 2018.
- 964 Irie, H., Kanaya, Y., Akimoto, H., Iwabuchi, H., Shimizu, a. and Aoki, K.: Dual-wavelength aerosol vertical profile
965 measurements by MAX-DOAS at Tsukuba, Japan, *Atmos. Chem. Phys.*, 9(2), 2741–2749, doi:10.5194/acp-8-341-
966 2008, 2009.
- 967 Irie, H., Takashima, H., Kanaya, Y., Boersma, K. F., Gast, L., Wittrock, F., Brunner, D., Zhou, Y. and Van
968 Roozendaal, M.: Eight-component retrievals from ground-based MAX-DOAS observations, *Atmos. Meas. Tech.*,
969 4(1), 1027–1044, doi:10.5194/amtd-4-639-2011, 2011.
- 970 Irie, H., Boersma, K. F., Kanaya, Y., Takashima, H., Pan, X., and Wang, Z. F.: Quantitative bias estimates for
971 tropospheric NO₂ columns retrieved from SCIAMACHY, OMI, and GOME-2 using a common standard for East
972 Asia, *Atmos. Meas. Tech.*, 5, 2403–2411, doi:10.5194/amt-5-2403-2012, 2012.



- 973 Irie, H., T. Nakayama, A. Shimizu, A. Yamazaki, T. Nagai, A. Uchiyama, Y. Zaizen, S. Kagamitani, and Y. Matsumi,
974 Evaluation of MAX-DOAS aerosol retrievals by coincident observations using CRDS, lidar, and sky radiometer in
975 Tsukuba, Japan, *Atmospheric Measurement Techniques*, 8, 2775–2788, doi:10.5194/amt-8-2775-2015, 2015.
- 976 Irie, H., Hoque, H. M. S., Damiani, A., Okamoto, H., Fatmi, A. M., Khatri, P., Takamura, T., and Jarupongsakul, T.:
977 Simultaneous observations by sky radiometer and MAX-DOAS for characterization of biomass burning plumes in
978 central Thailand in January–April 2016, *Atmos. Meas. Tech.*, 12, 599–606, <https://doi.org/10.5194/amt-12-599-2019>,
979 2019.
- 980 Jin, X., Fiore, A. M. A. M. A. M., Murray, L. T. L. T., Valin, L. C. L. C., Lamsal, L. N. L. N. L. N., Duncan, B.,
981 Folkert Boersma, K., De Smedt, I., Abad, G. G. G. G., Chance, K., others and Tonnesen, G. S. G. S.: Evaluating a
982 space-based indicator of surface ozone-NO_x-VOC sensitivity over mid-latitude source regions and application to
983 decadal trends, *J. Geophys. Res. Atmos.*, 122(19), 439–461, doi:10.1002/2017JD026720, 2017.
- 984 Jin, X., Fiore, A., Boersma, K. F., De Smedt, I. & Valin, L. Inferring changes in summertime surface ozone-NO_x-
985 VOC chemistry over U.S. urban areas from two decades of satellite and ground-based observations. *Environ. Sci.*
986 *Technol.* 54, 6518–6529, 2020.
- 987 Jung, Y., González Abad, G., Nowlan, C. R., Chance, K., Liu, X., Torres, O., & Ahn, C.: Explicit aerosol correction
988 of OMI formaldehyde retrievals. *Earth and Space Science*, 6, 2087–2105, <https://doi.org/10.1029/2019EA000702>,
989 2019.
- 990 Kaiser, J., Jacob, D. J., Zhu, L., Travis, K. R., Fisher, J. A., González Abad, G., Zhang, L., Zhang, X., Fried, A.,
991 Crounse, J. D., St. Clair, J. M., and Wisthaler, A.: High-resolution inversion of OMI formaldehyde columns to quantify
992 isoprene emission on ecosystem-relevant scales: application to the southeast US, *Atmos. Chem. Phys.*, 18, 5483–5497,
993 <https://doi.org/10.5194/acp-18-5483-2018>, 2018.
- 994 Khan, W. A., Khokhar, M. F., Shoaib, A. and Nawaz, R.: Monitoring and analysis of formaldehyde columns over
995 Rawalpindi-Islamabad, Pakistan using MAX-DOAS and satellite observation, *Atmos. Pollut. Res.*, (November 2017),
996 0–1, doi:10.1016/j.apr.2017.12.008, 2018.
- 997 Kleipool, Q. L., Dobber, M. R., de Haan, J. F., and Levelt, P. F.: Earth surface reflectance climatology from 3 years
998 of OMI data, *J. Geophys. Res.*, 113, D18308, <https://doi.org/10.1029/2008JD010290>, 2008.
- 999 Kleipool, Q., Ludewig, A., Babić, L., Bartstra, R., Braak, R., Dierssen, W., Dewitte, P.-J., Kenter, P., Landzaat, R.,
1000 Leloux, J., Loots, E., Meijering, P., van der Plas, E., Rozemeijer, N., Schepers, D., Schiavini, D., Smeets, J., Vacanti,
1001 G., Vonk, F., and Veefkind, P.: Pre-launch calibration results of the TROPOMI payload on-board the Sentinel-5
1002 Precursor satellite, *Atmos. Meas. Tech.*, 11, 6439–6479, <https://doi.org/10.5194/amt-11-6439-2018>, 2018.
- 1003 Kreher, K., Van Roozendaal, M., Hendrick, F., Apituley, A., Dimitropoulou, E., Frieß, U., Richter, A., Wagner, T.,
1004 Lampel, J., Abuhassan, N., Ang, L., Anguas, M., Bais, A., Benavent, N., Bösch, T., Bogner, K., Borovski, A.,
1005 Bruchkouski, I., Cede, A., Chan, K. L., Donner, S., Drosoglou, T., Fayt, C., Finkenzeller, H., Garcia-Nieto, D., Gielen,
1006 C., Gómez-Martín, L., Hao, N., Henzing, B., Herman, J. R., Hermans, C., Hoque, S., Irie, H., Jin, J., Johnston, P.,



- 1007 Khayyam Butt, J., Khokhar, F., Koenig, T. K., Kuhn, J., Kumar, V., Liu, C., Ma, J., Merlaud, A., Mishra, A. K.,
1008 Müller, M., Navarro-Comas, M., Ostendorf, M., Pazmino, A., Peters, E., Pinardi, G., Pinharanda, M., PETERS, A., Platt,
1009 U., Postlyakov, O., Prados-Roman, C., Puentedura, O., Querel, R., Saiz-Lopez, A., Schönhardt, A., Schreier, S. F.,
1010 Seyler, A., Sinha, V., Spinei, E., Strong, K., Tack, F., Tian, X., Tiefengraber, M., Tirpitz, J.-L., van Gent, J., Volkamer,
1011 R., Vrekoussis, M., Wang, S., Wang, Z., Wenig, M., Wittrock, F., Xie, P. H., Xu, J., Yela, M., Zhang, C., and Zhao,
1012 X.: Intercomparison of NO₂, O₄, O₃ and HCHO slant column measurements by MAX-DOAS and zenith-sky UV-
1013 visible spectrometers during CINDI-2, *Atmos. Meas. Tech.*, 13, 2169–2208, [https://doi.org/10.5194/amt-13-2169-](https://doi.org/10.5194/amt-13-2169-2020)
1014 2020, 2020.
- 1015 Kumar, V., Beirle, S., Dörner, S., Mishra, A. K., Donner, S., Wang, Y., Sinha, V., and Wagner, T.: Long-term MAX-
1016 DOAS measurements of NO₂, HCHO, and aerosols and evaluation of corresponding satellite data products over
1017 Mohali in the Indo-Gangetic Plain, *Atmos. Chem. Phys.*, 20, 14183–14235, [https://doi.org/10.5194/acp-20-14183-](https://doi.org/10.5194/acp-20-14183-2020)
1018 2020, 2020.
- 1019 Kwon, H.-A., Park, R. J., González Abad, G., Chance, K., Kurosu, T. P., Kim, J., Smedt, I. De, Roozendael, M. Van,
1020 Peters, E. and Burrows, J.: Description of a formaldehyde retrieval algorithm for the Geostationary Environment
1021 Monitoring Spectrometer (GEMS), *Atmos. Meas. Tech.*, 12(7), 3551–3571, 2019.
- 1022 Langen, J., Meijer, Y., Brinksma, E., Veihelmann, B., and Ingmann, P.: Copernicus Sentinels 4 and 5 Mission
1023 Requirements Traceability Document (MRTD), ESA, EOP-SM/2413/BV-bv , issue: 2, 2017.
- 1024 Levelt, P. F., van den Oord, G. H. ., Dobber, M. R., Malkki, A., Visser, H., de Vries, J., Stammes, P., Lundell, J. O. .
1025 and Saari, H.: The ozone monitoring instrument, *IEEE Trans. on Geosc. and Rem. Sens.*, 44(5), 1093–1101, 2006.
- 1026 Levelt, P. F., Joiner, J., Tamminen, J., Veefkind, J. P., Bhartia, P. K., Fioletov, V., Carn, S., Laat, J. De, Deland, M.,
1027 Marchenko, S. and Mcpeters, R.: The Ozone Monitoring Instrument : overview of 14 years in space, *Atmos. Chem.*
1028 *Phys.*, (18), 5699–5745, 2018.
- 1029 Levelt, P.F., Stein Zweers, Aben, Bauwens, Borsdorff, De Smedt, J. Eskes, Lerot, Loyola, Romahn, Stavrou, Theys,
1030 Van Roozendael, Veefkind, Verhoels: Air Quality Impacts of COVID-19 Lockdown Measures detected from space
1031 using high spatial resolution observations of multiple trace gases from Sentinel-5P/TROPOMI, to be submitted to
1032 ACP, 2021.
- 1033 Li, X., Brauers, T., Shao, M., Garland, R. M., Wagner, T., Deutschmann, T. and Wahner, A.: MAX-DOAS
1034 measurements in southern China: retrieval of aerosol extinctions and validation using ground-based in-situ data,
1035 *Atmos. Chem. Phys.*, 10(5), 2079–2089, doi:10.5194/acp-10-2079-2010, 2010.
- 1036 Li, C., Joiner, J., Krotkov, N. A., and Dunlap, L.: A new method for global retrievals of HCHO total columns from
1037 the Suomi National Polar-orbiting Partnership Ozone Mapping and Profiler Suite. *Geophys. Res. Lett.*, 42, 2515–
1038 2522. doi: 10.1002/2015GL063204, 2015.



- 1039 Li, K., Jacob, D. J., Shen, L., Lu, X., De Smedt, I., and Liao, H.: Increases in surface ozone pollution in China from
1040 2013 to 2019: anthropogenic and meteorological influences, *Atmos. Chem. Phys.*, 20, 11423–11433,
1041 <https://doi.org/10.5194/acp-20-11423-2020>, 2020.
- 1042 Lorente, A., Folkert Boersma, K., Yu, H., Dörner, S., Hilboll, A., Richter, A., Liu, M., Lamsal, L. N., Barkley, M.,
1043 De Smedt, I., Van Roozendaal, M., Wang, Y., Wagner, T., Beirle, S., Lin, J.-T., Krotkov, N., Stammes, P., Wang, P.,
1044
- 1045 Loyola, D. G., Xu, J., Heue, K.-P., and Zimmer, W.: Applying FP_ILM to the retrieval of geometry-dependent
1046 effective Lambertian equivalent reflectivity (GE_LER) daily maps from UVN satellite measurements, *Atmos. Meas.*
1047 *Tech.*, 13, 985–999, <https://doi.org/10.5194/amt-13-985-2020>, 2020.
- 1048 Eskes, H. J., and Krol, M.: Structural uncertainty in air mass factor calculation for NO₂ and HCHO satellite retrievals,
1049 *Atmos. Meas. Tech.*, 10, 759–782, <https://doi.org/10.5194/amt-10-759-2017>, 2017.
- 1050 Loyola, D. G., Gimeno García, S., Lutz, R., Argyrouli, A., Romahn, F., Spurr, R. J. D., Pedergnana, M., Doicu, A.,
1051 Molina García, V., and Schüssler, O.: The operational cloud retrieval algorithms from TROPOMI on board Sentinel-
1052 5 Precursor, *Atmos. Meas. Tech.*, 11, 409–427, <https://doi.org/10.5194/amt-11-409-2018>, 2018.
- 1053 Ludewig, A., Kleipool, Q., Bartstra, R., Landzaat, R., Leloux, J., Loots, E., Meijering, P., van der Plas, E., Rozemeijer,
1054 N., Vonk, F., and Veefkind, P.: In-flight calibration results of the TROPOMI payload on board the Sentinel-5
1055 Precursor satellite, *Atmos. Meas. Tech.*, 13, 3561–3580, <https://doi.org/10.5194/amt-13-3561-2020>, 2020.
- 1056 Ma, J. Z., Beirle, S., Jin, J. L., Shaiganfar, R., Yan, P., and Wagner, T.: Tropospheric NO₂ vertical column densities
1057 over Beijing: results of the first three years of ground-based MAX-DOAS measurements (2008–2011) and satellite
1058 validation, *Atmos. Chem. Phys.*, 13, 1547–1567, doi:10.5194/acp-13-1547-2013, 2013.
- 1059 Mahajan, A. S., De Smedt, I., Biswas, M. S., Ghude, S., Fadnavis, S., Roy, C. and van Roozendaal, M.: Inter-annual
1060 variations in satellite observations of nitrogen dioxide and formaldehyde over India, *Atmos. Environ.*, 116, 194–201,
1061 doi:10.1016/j.atmosenv.2015.06.004, 2015.
- 1062 Marais, E. A., Jacob, D. J., Kurosu, T. P., Chance, K., Murphy, J. G., Reeves, C., Mills, G., Casadio, S., Millet, D. B.,
1063 Barkley, M. P., Paulot, F., et al.: Isoprene emissions in Africa inferred from OMI observations of formaldehyde
1064 columns, *Atmos. Chem. Phys. Discuss.*, 12(3), 7475–7520, doi:10.5194/acpd-12-7475-2012, 2012.
- 1065 Marbach, T., Beirle, S., Platt, U., Hoor, P., Wittrock, F., Richter, A., Vrekoussis, M., Grzegorski, M., Burrows, J. P.
1066 and Wagner, T.: Satellite measurements of formaldehyde linked to shipping emissions, *Atmos. Chem. Phys.*, 9(21),
1067 8223–8234, doi:10.5194/acp-9-8223-2009, 2009.
- 1068 Meller, R. and Moortgat, G. K.: Temperature dependence of the absorption cross section of HCHO between 223 and
1069 323 K in the wavelength range 225–375 nm, *J. Geophys. Res.*, 105, 7089–7102,
1070 <https://doi.org/10.1029/1999JD901074>, 2000.



- 1071 Millet, D. B., Jacob, D. J., Boersma, K. F., Fu, T.-M., Kurosu, T. P., Chance, K. V., Heald, C. L. and Guenther, A.:
1072 Spatial distribution of isoprene emissions from North America derived from formaldehyde column measurements by
1073 the OMI satellite sensor, *Journal of Geophysical Research*, 113(D2), 1-18, doi:10.1029/2007JD008950, 2008.
- 1074 Nightingale, J., Boersma, K., Muller, J.-P., Compornolle, S., Lambert, J.-C., Blessing, S., Giering, R., Gobron, N., De
1075 Smedt, I., Coheur, P. and others: Quality assurance framework development based on six new ECV data products to
1076 enhance user confidence for climate applications, *Remote Sens.*, 10(8), 1254, 2018.
- 1077 Opacka, B., Müller, J.-F., Stavrou, T., Bauwens, M., Sindelarova, K., Markova, J., and Guenther, A. B.: Global and
1078 regional impacts of land cover changes on isoprene emissions derived from spaceborne data and the MEGAN model,
1079 *Atmos. Chem. Phys. Discuss.* [preprint], <https://doi.org/10.5194/acp-2021-95>, in review, 2021.
- 1080 Palmer, P. I., Jacob, D. J., Chance, K. V., Martin, R. V., D, R. J., Kurosu, T. P., Bey, I., Yantosca, R. and Fiore, A.:
1081 Air mass factor formulation for spectroscopic measurements from satellites: Application to formaldehyde retrievals
1082 from the Global Ozone Monitoring Experiment, *Journal of Geophysical Research*, 106(D13), 14539-14550,
1083 doi:10.1029/2000JD900772, 2001.
- 1084 Pinardi, G., Van Roozendaal, M., Abuhassan, N., Adams, C., Cede, A., Clémer, K., Fayt, C., Frieß, U., Gil, M.,
1085 Herman, J., Hermans, C., Hendrick, F., Irie, H., Merlaud, A., Navarro Comas, M., Peters, E., Piter, A. J. M.,
1086 Puentedura, O., Richter, A., Schönhardt, A., Shaiganfar, R., Spinei, E., Strong, K., Takashima, H., Vrekoussis, M.,
1087 Wagner, T., Wittrock, F., and Yilmaz, S.: MAX-DOAS formaldehyde slant column measurements during CINDI:
1088 inter-comparison and analysis improvement, *Atmos. Meas. Tech.*, 6, 167-185, doi:10.5194/amt-6-167-2013, 2013.
- 1089 Platt, U and Stutz, J.: *Differential Optical Absorption Spectroscopy: Principles and Applications (Physics of Earth and
1090 Space Environments)*, Springer-Verlag, Berlin, Heidelberg, ISBN 978-3540211938, 2008.
- 1091 Richter, A., Eyring, V., Burrows, J. P., Bovensmann, H., Lauer, A., Sierk, B., and Crutzen, P. J., Satellite
1092 measurements of NO₂ from international shipping emissions, *Geophys. Res. Lett.*, 31, L23110,
1093 doi:10.1029/2004GL020822, 2004.
- 1094 Richter, A., Begoin, M., Hilboll, A. and Burrows, J.P.: An improved NO₂ retrieval for the GOME-2 satellite
1095 instrument, *Atmos. Meas. Tech.*, 4(1), 1147–1159, doi:10.5194/amtd-4-213-2011, 2011.
- 1096 Richter, A., Hilboll, A., Sanders, A., Peters, E. and Burrows, J.P.: Inhomogeneous scene effects in OMI NO₂
1097 observations, *Geophysical Research Abstracts*, EGU General Assembly 2018, Vol. 20, EGU2018-9630-3,
1098 <https://meetingorganizer.copernicus.org/EGU2018/EGU2018-9630-3.pdf>, 2018. Richter, A., Hilboll, A., Sanders, A.
1099 and Burrows, J.P.: Inhomogeneous scene effects in TROPOMI satellite data, 9th DOAS Workshop, 13-15 July 2020,
1100 Utrecht, 2020.
- 1101 Rivera Cárdenas, C., Guarín, C., Stremme, W., Friedrich, M. M., Bezanilla, A., Rivera Ramos, D., Mendoza-
1102 Rodríguez, C. A., Grutter, M., Blumenstock, T., and Hase, F.: Formaldehyde total column densities over Mexico City:
1103 comparison between multi-axis differential optical absorption spectroscopy and solar-absorption Fourier transform
1104 infrared measurements, *Atmos. Meas. Tech.*, 14, 595–613, <https://doi.org/10.5194/amt-14-595-2021>, 2021.



- 1105 Rodgers, C. D.: Inverse Methods for Atmospheric Sounding, Theory and Practice, World Scientific Publishing,
1106 Singapore-New-Jersey-London-Hong Kong, 2000.
- 1107 Rodgers, C. D., and B. J. Connor: Intercomparison of remote sounding instruments, *J. Geophys. Res.*, 108,
1108 doi:10.1029/2002JD002299, 2003.
- 1109 Ryan, R. G., Silver, J. D., Querel, R., Smale, D., Rhodes, S., Tully, M., Jones, N., and Schofield, R.: Comparison of
1110 formaldehyde tropospheric columns in Australia and New Zealand using MAX-DOAS, FTIR and TROPOMI, *Atmos.*
1111 *Meas. Tech. Discuss.*, <https://doi.org/10.5194/amt-2020-232>, in review, 2020.
- 1112 Sen, P. K.: Estimates of the regression coefficient based on Kendall's tau, *J. Am. Stat. Assoc.*, 63, 1379–1389,
1113 <https://doi.org/10.2307/2285891>, 1968.
- 1114 Shen, L., Jacob, D. J., Zhu, L., Zhang, Q., Zheng, B., Sulprizio, M. P., Li, K., De Smedt, I., González Abad, G., Cao,
1115 H. and others: The 2005–2016 trends of formaldehyde columns over China observed by satellites: Increasing
1116 anthropogenic emissions of volatile organic compounds and decreasing agricultural fire emissions, *Geophys. Res.*
1117 *Lett.*, 46(8), 4468–4475, 2019.
- 1118 Sinreich, R., Frieß, U., Wagner, T., and Platt, U.: Multi axis differential optical absorption spectroscopy (MAX-
1119 DOAS) of gas and aerosol distributions, *Faraday Discuss.*, 130, 153–164, <https://doi.org/10.1039/B419274P>, 2005.
- 1120 Song, C. H., Kim, H. S., von Glasow, R., Brimblecombe, P., Kim, J., Park, R. J., Woo, J. H., and Kim, Y. H.: Source
1121 identification and budget analysis on elevated levels of formaldehyde within the ship plumes: a ship-plume
1122 photochemical/dynamic model analysis, *Atmos. Chem. Phys.*, 10, 11969–11985, [https://doi.org/10.5194/acp-10-](https://doi.org/10.5194/acp-10-11969-2010)
1123 [11969-2010](https://doi.org/10.5194/acp-10-11969-2010), 2010
- 1124 Souri, A. H., Nowlan, C. R., Wolfe, G. M., Lamsal, L. N., Chan Miller, C. E., Abad, G. G., Janz, S. J., Fried, A.,
1125 Blake, D. R., Weinheimer, A. J., Diskin, G. S., Liu, X. and Chance, K.: Revisiting the effectiveness of HCHO/NO₂
1126 ratios for inferring ozone sensitivity to its precursors using high resolution airborne remote sensing observations in a
1127 high ozone episode during the KORUS-AQ campaign, *Atmos. Environ.*, 224, 117341,
1128 doi:<https://doi.org/10.1016/j.atmosenv.2020.117341>, 2020.
- 1129 Spurr, R. J. D.: LIDORT and VLIDORT: Linearized pseudo-spherical scalar and vector discrete ordinate radiative
1130 transfer models for use in remote sensing retrieval problems, in *Light Scattering Reviews*, edited by: Kokhanovsky,
1131 A., 229–271, Berlin, 2008.
- 1132 Stavroukou, T., Müller, J.-F., Bauwens, M., De Smedt, I., Van Roozendaal, M., Guenther, A., Wild, M. and Xia, X.:
1133 Isoprene emissions over Asia 1979–2012: impact of climate and land-use changes, *Atmos. Chem. Phys.*, 14(9), 4587–
1134 4605, 2014.
- 1135 Stavroukou, T., Müller, J.-F., Bauwens, M., De Smedt, I., Van Roozendaal, M., De Mazière, M., Vigouroux, C.,
1136 Hendrick, F., George, M., Clerbaux, C., Coheur, P.-F., and Guenther, A.: How consistent are top-down hydrocarbon
1137 emissions based on formaldehyde observations from GOME-2 and OMI?, *Atmos. Chem. Phys.*, 15, 11861–11884,
1138 <https://doi.org/10.5194/acp-15-11861-2015>, 2015.



- 1139 Stavrakou, T., Müller, J.-F., Bauwens, M., De Smedt, I., Lerot, C., Van Roozendael, M., Coheur, P.-F., Clerbaux, C.,
1140 Boersma, K. F., van der A, R. and Song, Y.: Substantial Underestimation of Post-Harvest Burning Emissions in the
1141 North China Plain Revealed by Multi-Species Space Observations, *Sci. Rep.*, 6(1), 32307, doi:10.1038/srep32307,
1142 2016.
- 1143 Stavrakou, T., Müller, J.-F., Bauwens, M., De Smedt, I., Van Roozendael, M. and Guenther, A.: Impact of Short-Term
1144 Climate Variability on Volatile Organic Compounds Emissions Assessed Using OMI Satellite Formaldehyde
1145 Observations, *Geophys. Res. Lett.*, 45(16), 8681–8689, 2018.
- 1146 Su, W., Liu, C., Hu, Q., Zhao, S., Sun, Y., Wang, W., Zhu, Y., Liu, J., and Kim, J.: Primary and secondary sources of
1147 ambient formaldehyde in the Yangtze River Delta based on Ozone Mapping and Profiler Suite (OMPS) observations,
1148 *Atmos. Chem. Phys.*, 19, 6717–6736, <https://doi.org/10.5194/acp-19-6717-2019>, 2019.
- 1149 Su, W., Liu, C., Chan, K. L., Hu, Q., Liu, H., Ji, X., Zhu, Y., Liu, T., Zhang, C., Chen, Y., and Liu, J.: An improved
1150 TROPOMI tropospheric HCHO retrieval over China, *Atmos. Meas. Tech.*, 13, 6271–6292,
1151 <https://doi.org/10.5194/amt-13-6271-2020>, 2020.
- 1152 Sun, W., Zhu, L., De Smedt, I., Bai, B., Pu, D., Chen, Y., et al.: Global significant changes in formaldehyde (HCHO)
1153 columns observed from space at the early stage of the COVID-19 pandemic. *Geophysical Research Letters*, 48,
1154 e2020GL091265. <https://doi.org/10.1029/2020GL091265>, 2021.
- 1155 Surl, L., Palmer, P. I., and González Abad, G.: Which processes drive observed variations of HCHO columns over
1156 India?, *Atmos. Chem. Phys.*, 18, 4549–4566, <https://doi.org/10.5194/acp-18-4549-2018>, 2018.
- 1157 Theys, N., De Smedt, I., van Gent, J., Danckaert, T., Wang, T., Hendrick, F., Stavrakou, T., Bauduin, S., Clarisse, L.,
1158 Li, C., Krotkov, N., Yu, H., Brenot, H. and Van Roozendael, M.: Sulfur dioxide vertical column DOAS retrievals
1159 from the Ozone Monitoring Instrument: Global observations and comparison to ground-based and satellite data, *J.*
1160 *Geophys. Res. Atmos.*, 120(6), 2014JD022657, doi:10.1002/2014JD022657, 2015.
- 1161 Theys, N., Volkamer, R., Müller, J. F., Zarzana, K. J., Kille, N., Clarisse, L., De Smedt, I., Lerot, C., Finkenzeller, H.,
1162 Hendrick, F., Koenig, T. K., Lee, C. F., Knote, C., Yu, H. and Van Roozendael, M.: Global nitrous acid emissions and
1163 levels of regional oxidants enhanced by wildfires, *Nat. Geosci.*, 13(10), 681–686, doi:10.1038/s41561-020-0637-7,
1164 2020.
- 1165 Tirpitz, J.-L., Frieß, U., Hendrick, F., Alberti, C., Allaart, M., Apituley, A., Bais, A., Beirle, S., Berkhout, S., Bognar,
1166 K., Bösch, T., Bruchkouski, I., Cede, A., Chan, K. L., den Hoed, M., Donner, S., Drosoglou, T., Fayt, C., Friedrich,
1167 M. M., Frumau, A., Gast, L., Gielen, C., Gomez-Martín, L., Hao, N., Hensen, A., Henzing, B., Hermans, C., Jin, J.,
1168 Kreher, K., Kuhn, J., Lampel, J., Li, A., Liu, C., Liu, H., Ma, J., Merlaud, A., Peters, E., Pinardi, G., PETERS, A., Platt,
1169 U., Puentedura, O., Richter, A., Schmitt, S., Spinei, E., Stein Zweers, D., Strong, K., Swart, D., Tack, F., Tiefengraber,
1170 M., van der Hoff, R., van Roozendael, M., Vlemmix, T., Vonk, J., Wagner, T., Wang, Y., Wang, Z., Wenig, M.,
1171 Wiegner, M., Witrock, F., Xie, P., Xing, C., Xu, J., Yela, M., Zhang, C., and Zhao, X.: Intercomparison of MAX-
1172 DOAS vertical profile retrieval algorithms: studies on field data from the CINDI-2 campaign, *Atmos. Meas. Tech.*,
1173 14, 1–35, <https://doi.org/10.5194/amt-14-1-2021>, 2021.



- 1174 van Geffen, J., Boersma, K. F., Eskes, H., Sneep, M., ter Linden, M., Zara, M., and Veefkind, J. P.: S5P TROPOMI
1175 NO₂ slant column retrieval: method, stability, uncertainties and comparisons with OMI, *Atmos. Meas. Tech.*, 13,
1176 1315–1335, <https://doi.org/10.5194/amt-13-1315-2020>, 2020.
- 1177 Veefkind, J. P., Aben, I., McMullan, K., Förster, H., de Vries, J., Otter, G., Claas, J., Eskes, H. J., de Haan, J. F.,
1178 Kleipool, Q., van Weele, M., et al.: TROPOMI on the ESA Sentinel-5 Precursor: A GMES mission for global
1179 observations of the atmospheric composition for climate, air quality and ozone layer applications, *Remote Sensing of*
1180 *Environment*, 120(0), 70-83, 2012.
- 1181 Veefkind, J. P., de Haan, J. F., Sneep, M., and Levelt, P. F.: Improvements to the OMI O₂–O₂ operational cloud
1182 algorithm and comparisons with ground-based radar–lidar observations, *Atmos. Meas. Tech.*, 9, 6035-6049,
1183 <https://doi.org/10.5194/amt-9-6035-2016>, 2016.
- 1184 Verhoelst, T., Compernelle, S., Pinardi, G., Lambert, J.-C., Eskes, H. J., Eichmann, K.-U., Fjæraa, A. M., Granville,
1185 J., Niemeijer, S., Cede, A., Tiefengraber, M., Hendrick, F., Pazmiño, A., Bais, A., Bazureau, A., Boersma, K. F.,
1186 Bogner, K., Dehn, A., Donner, S., Elokhov, A., Gebetsberger, M., Goutail, F., Grutter de la Mora, M., Gruzdev, A.,
1187 Gratsea, M., Hansen, G. H., Irie, H., Jepsen, N., Kanaya, Y., Karagkiozidis, D., Kivi, R., Kreher, K., Levelt, P. F.,
1188 Liu, C., Müller, M., Navarro Comas, M., PETERS, A. J. M., Pommereau, J.-P., Portafaix, T., Prados-Roman, C.,
1189 Puentedura, O., Querel, R., Remmers, J., Richter, A., Rimmer, J., Rivera Cárdenas, C., Saavedra de Miguel, L.,
1190 Sinyakov, V. P., Stremme, W., Strong, K., Van Roozendaal, M., Veefkind, J. P., Wagner, T., Wittrock, F., Yela
1191 González, M., and Zehner, C.: Ground-based validation of the Copernicus Sentinel-5P TROPOMI NO₂ measurements
1192 with the NDACC ZSL-DOAS, MAX-DOAS and Pandonia global networks, *Atmos. Meas. Tech.*, 14, 481–510,
1193 <https://doi.org/10.5194/amt-14-481-2021>, 2021.
- 1194 Vigouroux, C., Hendrick, F., Stavrou, T., Dils, B., De Smedt, I., Hermans, C., Merlaud, A., Scolas, F., Senten, C.,
1195 Vanhaelewyn, G., Fally, S., Carleer, M., Metzger, J.-M., Müller, J.-F., Van Roozendaal, M., and De Mazière, M.:
1196 Ground-based FTIR and MAX-DOAS observations of formaldehyde at Réunion Island and comparisons with satellite
1197 and model data, *Atmos. Chem. Phys.*, 9, 9523-9544, doi:10.5194/acp-9-9523-2009, 2009.
- 1198 Vigouroux, C., Bauer Aquino, C. A., Bauwens, M., Becker, C., Blumenstock, T., De Mazière, M., García, O., Grutter,
1199 M., Guarin, C., Hannigan, J., Hase, F., Jones, N., Kivi, R., Koshelev, D., Langerock, B., Lutsch, E., Makarova, M.,
1200 Metzger, J.-M., Müller, J.-F., Notholt, J., Ortega, I., Palm, M., Paton-Walsh, C., Poberovskii, A., Rettinger, M.,
1201 Robinson, J., Smale, D., Stavrou, T., Stremme, W., Strong, K., Sussmann, R., Té, Y., and Toon, G.: NDACC
1202 harmonized formaldehyde time series from 21 FTIR stations covering a wide range of column abundances, *Atmos.*
1203 *Meas. Tech.*, 11, 5049–5073, <https://doi.org/10.5194/amt-11-5049-2018>, 2018.
- 1204 Vigouroux, C., Langerock, B., Bauer Aquino, C. A., Blumenstock, T., Cheng, Z., De Mazière, M., De Smedt, I.,
1205 Grutter, M., Hannigan, J. W., Jones, N., Kivi, R., Loyola, D., Lutsch, E., Mahieu, E., Makarova, M., Metzger, J.-M.,
1206 Morino, I., Murata, I., Nagahama, T., Notholt, J., Ortega, I., Palm, M., Pinardi, G., Röhling, A., Smale, D., Stremme,
1207 W., Strong, K., Sussmann, R., Té, Y., van Roozendaal, M., Wang, P., and Winkler, H.: TROPOMI–Sentinel-5



- 1208 Precursor formaldehyde validation using an extensive network of ground-based Fourier-transform infrared stations,
1209 Atmos. Meas. Tech., 13, 3751–3767, <https://doi.org/10.5194/amt-13-3751-2020>, 2020.
- 1210 Vlemmix, T., Pitters, A., Stammes, P., Wang, P. and Levelt, P. F.: Retrieval of tropospheric NO₂ using the MAX-
1211 DOAS method combined with relative intensity measurements for aerosol correction, Atmos. Meas. Tech., 3(5),
1212 1287–1305, doi:10.5194/amt-3-1287-2010, 2010.
- 1213 Vlemmix, T., Hendrick, F., Pinardi, G., Smedt, I. De, Fayt, C., Hermans, C., Pitters, A., Wang, P. and Levelt, P.: MAX-
1214 DOAS observations of aerosols, formaldehyde and nitrogen dioxide in the Beijing area: comparison of two profile
1215 retrieval, Atmos. Meas. Tech., (2), 941–963, doi:10.5194/amt-8-941-2015, 2015.
- 1216 Vrekoussis, M., Wittrock, F., Richter, A. and Burrows, J. P.: GOME-2 observations of oxygenated VOCs: what can
1217 we learn from the ratio glyoxal to formaldehyde on a global scale?, Atmos. Chem. Phys., 10(21), 10145-10160, 2010.
- 1218 Wagner, T., Dix, B., Friedeburg, C. Von, Friess, U., Sanghavi, S., Sinreich, R. and Platt, U.: MAX-DOAS O₄
1219 measurements: a new technique to derive information on atmospheric aerosols - Principles and information content,
1220 J. Geophys. Res., 109(D22205), 2004.
- 1221 Wagner, T., Beirle, S., Brauers, T., Deutschmann, T., Frieß, U., Hak, C., Halla, J. D., Heue, K. P., Junkermann, W.,
1222 Li, X., Platt, U., and Pundt-Gruber, I.: Inversion of tropospheric profiles of aerosol extinction and HCHO and NO₂
1223 mixing ratios from MAX-DOAS observations in Milano during the summer of 2003 and comparison with independent
1224 data sets, Atmos. Meas. Tech., 4, 2685-2715, doi:10.5194/amt-4-2685-2011, 2011.
- 1225 Wang, Y., Beirle, S., Hendrick, F., Hilboll, A., Jin, J., Kyuberis, A. A., Lampel, J., Li, A., Luo, Y., Lodi, L., Ma, J.,
1226 Navarro, M., Ortega, I., Peters, E., Polyansky, O. L., Remmers, J., Richter, A., Puentedura, O., Van Roozendaal, M.,
1227 Seyler, A., Tennyson, J., Volkamer, R., Xie, P., Zobov, N. F., and Wagner, T.: MAX-DOAS measurements of HONO
1228 slant column densities during the MAD-CAT campaign: inter-comparison, sensitivity studies on spectral analysis
1229 settings, and error budget, Atmos. Meas. Tech., 10, 3719–3742, <https://doi.org/10.5194/amt-10-3719-2017>, 2017.
- 1230 Wang, Y., Dörner, S., Donner, S., Böhnke, S., Smedt, I. De, Dickerson, R. R., Dong, Z., He, H., Li, Z., Li, Z. and
1231 others: Vertical profiles of NO₂, SO₂, HONO, HCHO, CHOCHO and aerosols derived from MAX-DOAS
1232 measurements at a rural site in the central western North China Plain and their relation to emission sources and effects
1233 of regional transport, Atmos. Chem. Phys., 19(8), 5417–5449, 2019a.
- 1234 Wang, Y., Wang, Z., Yu, C., Zhu, S., Cheng, L., Zhang, Y. and Chen, L.: Validation of OMI HCHO Products Using
1235 MAX-DOAS observations from 2010 to 2016 in Xianghe, Beijing: Investigation of the Effects of Aerosols on Satellite
1236 Products, Remote Sens., 11(2), 203, doi:10.3390/rs11020203, 2019b.
- 1237 Wells, K. C., Millet, D. B., Payne, V. H., Deventer, M. J., Bates, K. H., Gouw, J. A., Graus, M., Warneke, C.,
1238 Wisthaler, A. and Fuentes, J. D.: Satellite isoprene retrievals constrain emissions and atmospheric oxidation, Nature,
1239 585(August 2019), doi:10.1038/s41586-020-2664-3, 2020.



- 1240 Williams, J. E., Boersma, K. F., Le Sager, P., and Verstraeten, W. W.: The high-resolution version of TM5-MP for
1241 optimized satellite retrievals: description and validation, *Geosci. Model Dev.*, 10, 721–750,
1242 <https://doi.org/10.5194/gmd-10-721-2017>, 2017.
- 1243 Wittrock, F., Oetjen, H., Richter, A., Fietkau, S., Medeke, T., Rozanov, A., and Burrows, J.P.: MAX-DOAS
1244 measurements of atmospheric trace gases in Ny-Alesund – Radiative transfer studies and their application, *Atmos.*
1245 *Chem. Phys.*, 4, 955–966, doi:10.5194/acp-4-955-2004, 2004.
- 1246 Wittrock, F., Richter, A., Oetjen, H., Burrows, J. P., Kanakidou, M., Myriokefalitakis, S., Volkamer, R., Beirle, S.,
1247 Platt, U. and Wagner, T.: Simultaneous global observations of glyoxal and formaldehyde from space, *Geophysical*
1248 *Research Letters*, 33(16), 1-5, doi:10.1029/2006GL026310, 2006.
- 1249 Zara, M., Boersma, K. F., De Smedt, I., Richter, A., Peters, E., van Geffen, J. H. G. M., Beirle, S., Wagner, T., Van
1250 Roozendaal, M., Marchenko, S., Lamsal, L. N., and Eskes, H. J.: Improved slant column density retrieval of nitrogen
1251 dioxide and formaldehyde for OMI and GOME-2A from QA4ECV: intercomparison, uncertainty characterisation,
1252 and trends, *Atmos. Meas. Tech.*, 11, 4033–4058, <https://doi.org/10.5194/amt-11-4033-2018>, 2018.
- 1253 Zhu, L., Jacob, D. J., Kim, P. S., Fisher, J. A., Yu, K., Travis, K. R., Mickleby, L. J., Yantosca, R. M., Sulprizio, M. P.,
1254 De Smedt, I., González Abad, G., Chance, K., Li, C., Ferrare, R., Fried, A., Hair, J. W., Hanisco, T. F., Richter, D.,
1255 Jo Scarino, A., Walega, J., Weibring, P., and Wolfe, G. M.: Observing atmospheric formaldehyde (HCHO) from
1256 space: validation and intercomparison of six retrievals from four satellites (OMI, GOME2A, GOME2B, OMPS) with
1257 SEAC4RS aircraft observations over the southeast US, *Atmos. Chem. Phys.*, 16, 13477–13490,
1258 <https://doi.org/10.5194/acp-16-13477-2016>, 2016.
- 1259 Zhu, L., González Abad, G., Nowlan, C. R., Chan Miller, C., Chance, K., Apel, E. C., DiGangi, J. P., Fried, A.,
1260 Hanisco, T. F., Hornbrook, R. S., Hu, L., Kaiser, J., Keutsch, F. N., Permar, W., St. Clair, J. M., and Wolfe, G. M.:
1261 Validation of satellite formaldehyde (HCHO) retrievals using observations from 12 aircraft campaigns, *Atmos. Chem.*
1262 *Phys.*, 20, 12329–12345, <https://doi.org/10.5194/acp-20-12329-2020>, 2020.
- 1263 Zyrichidou, I., Balis, D., Koukouli, M. E., Drosoglou, T., Bais, A., Gratsea, M., Gerasopoulos, E., Liora, N., Poupkou,
1264 A., Giannaros, C. and others: Adverse results of the economic crisis: A study on the emergence of enhanced
1265 formaldehyde (HCHO) levels seen from satellites over Greek urban sites, *Atmos. Res.*, 224, 42–51, 2019.